DISSERTATIONES
SCIENTIAE
MATERIALIS
UNIVERSITATIS
TARTUENSIS
30

HELINA SEEMEN

Atomic layer deposition and microscopic analysis of magnetically and electrically polarizable thin solid films

DISSERTATIONES SCIENTIAE MATERIALIS UNIVERSITATIS TARTUENSIS

30

DISSERTATIONES SCIENTIAE MATERIALIS UNIVERSITATIS TARTUENSIS
30

HELINA SEEMEN

Atomic layer deposition and microscopic analysis of magnetically and electrically polarizable thin solid films

UNIVERSITY OF TARTU
Press

The study was carried out at the Institute of Physics, University of Tartu, Estonia.

The Dissertation was admitted on May 19, 2021, in partial fulfilment of the requirements for the degree of Doctor of Philosophy in Material Science and allowed for defence by the Scientific Council on Material Science of the Faculty of Science and Technology, University of Tartu.

Supervisors:	Aile Tamm (PhD), associate professor, Institute of Physics, University of Tartu, Tartu, Estonia.
	Kaupo Kukli (PhD), professor, Institute of Physics, University of Tartu, Tartu, Estonia.
Opponents:	Jyrki Räisänen (PhD), professor emeritus, Department of Physics, University of Helsinki, Helsinki, Finland.
	Olga Volobujeva (PhD), senior researcher, Department of Materials and Environmental Technology, Tallinn University of Technology, Tallinn, Estonia.
Commencement:	August 26, 2021, at the University of Tartu, Tartu, Estonia

This work has been partially supported by the European Regional Development Fund project “Emerging orders in quantum and nanomaterials” (TK134), Estonian Research Agency (IUT2-24, IUT23-7, PRG4, PRG753), Estonian Academy of Sciences (SLTFYPROF), Spanish Ministry of Economy and Competitiveness (TEC2014-52152-C3-3-R, TEC2017-84321-C4-2-R) with support of Feder funds, and the Finnish Centre of Excellence in Atomic Layer Deposition (284623).

European Union
European Regional
Development Fund

Investing
in your future

ISSN 2228-0928
ISBN 978-9949-03-640-0 (print)
ISBN 978-9949-03-641-7 (pdf)

University of Tartu Press
www.tyk.ee

TABLE OF CONTENTS

LIST OF ORIGINAL PUBLICATIONS AND AUTHOR'S CONTRIBUTIONS

This Thesis is based on the following publications referred to in the text by their corresponding Roman numerals I–V:

I. **H. Seemen**, K. Kukli, T. Jõgiaas, P. Ritslaid, J. Link, R. Stern, S. Dueñas, H. Castán, A. Tamm, Properties of atomic layer deposited iron oxide and bismuth oxide chloride structures, *Journal of Alloys and Compounds*, 846 (2020) 156099. https://doi.org/10.1016/j.jallcom.2020.156099
The author contributed to this article by preparing the samples using an atomic layer deposition method. The author characterized the samples using scanning electron microscopy, energy-dispersive X-ray spectrometry, X-ray fluorescence spectroscopy and vibrating sample magnetometry. The author gathered and analysed the experimental data and formulated it into a scientific paper.

II. A. Tamm, K. Kalam, **H. Seemen**, J. Kozlova, K. Kukli, J. Aarik, Magnetic and electrical performance of atomic layer deposited iron erbium oxide thin films, *ACS Omega*, 2 (12) (2017) 8836–8842. https://doi.org/10.1021/acsomega.7b01394
The author contributed to this article by investigating the morphology of the samples using scanning electron microscopy and by participating in reviewing and proofreading process of the written scientific paper.

III. **H. Seemen**, M. Rähn, K. Kalam, T. Sajavaara, S. Dueñas, H. Castán, J. Link, R. Stern, K. Kukli, A. Tamm, Properties of atomic layer deposited nanolaminates of zirconium and cobalt oxides, *ECS Journal of Solid State Science and Technology*, 7 (8) (2018) P402–P409. https://doi.org/10.1149/2.0191808jss
The author contributed to this article by preparing the samples using an atomic layer deposition method and preparing the lamellae-type samples for transmission electron microscopy studies using the dual-beam scanning electron microscopy device equipped with a focused ion beam module. The author characterized the samples using scanning electron microscopy, X-ray fluorescence spectroscopy and vibrating sample magnetometry. The author gathered and analysed the experimental data and formulated it into a scientific paper.

IV. K. Kukli, M. Kemell, H. Castán, S. Dueñas, **H. Seemen**, M. Rähn, J. Link, R. Stern, M. J. Heikkilä, M. Ritala, M. Leskelä, Atomic layer deposition and performance of ZrO_2-Al_2O_3 thin films, *ECS Journal of Solid State Science and Technology*, 7 (5) (2018) P287–P294. https://doi.org/10.1149/2.0021806jss
The author contributed to this article by preparing lamellae out of the atomic layer deposited samples for transmission electron microscopy studies using

the dual-beam scanning electron microscope equipped with a focused ion beam module, by writing the lamellae creation section and participating in reviewing and proofreading process of the written scientific paper.

V. K. Kukli, M. Kemell, H. Castán, S. Dueñas, **H. Seemen**, M. Rähn, J. Link, R. Stern, M. Ritala, M. Leskelä, Atomic layer deposition and properties of HfO_2-Al_2O_3 nanolaminates, *ECS Journal of Solid State Science and Technology*, 7 (9) (2018) P501–P508. https://doi.org/10.1149/2.0261809jss
The author contributed to this article by preparing lamella out of the atomic layer deposited sample for transmission electron microscopy studies using the dual-beam scanning electron microscope equipped with a focused ion beam module. The author also participated in the reviewing and proofreading process of the written scientific paper.

LIST OF AUTHOR'S OTHER PUBLICATIONS

1. A. Tamm, A. Tarre, V. Verchenko, **H. Seemen**, R. Stern, Atomic layer deposition of superconducting CuO thin films on three-dimensional substrates, *Crystals*, 10 (2020) 650. https://doi.org/10.3390/cryst10080650
2. K. Kukli, M. Mikkor, A. Šutka, M. Kull, **H. Seemen**, J. Link, R. Stern, A. Tamm, Behavior of nanocomposite consisting of manganese ferrite particles and atomic layer deposited bismuth oxide chloride film, *Journal of Magnetism and Magnetic Materials*, 498 (2020) 166167. https://doi.org/10.1016/j.jmmm.2019.166167
3. T. Jõgiaas, M. Kull, **H. Seemen**, P. Ritslaid, K. Kukli, A. Tamm, Optical and mechanical properties of nanolaminates of zirconium and hafnium oxides grown by atomic layer deposition, *Journal of Vacuum Science & Technology A*, 38 (2020) 022406. https://doi.org/10.1116/1.5131563
4. K. Kalam, **H. Seemen**, M. Mikkor, T. Jõgiaas, P. Ritslaid, A. Tamm, K. Kukli, A. Kasikov, J. Link, R. Stern, S. Dueñas, H. Castán, Electrical and magnetic properties of atomic layer deposited cobalt oxide and zirconium oxide nanolaminates, *Thin Solid Films*, 669 (2019) 294–300. https://doi.org/10.1016/j.tsf.2018.11.008
5. S. Dueñas, H. Castán, H. García, Ó. G. Ossorio, L. A. Domínguez, **H. Seemen**, A. Tamm, K. Kukli, J. Aarik, The role of defects in the resistive switching behavior of Ta_2O_5-TiO_2-based metal–insulator–metal (MIM) devices for memory applications, *Journal of Electronic Materials*, 47 (2018) 4938–4943. https://doi.org/10.1007/s11664-018-6105-0
6. A. Kasikov, T. Kahro, L. Matisen, M. Kodu, A. Tarre, **H. Seemen**, H. Alles, The optical properties of transferred graphene and the dielectrics grown on it obtained by ellipsometry, *Applied Surface Science*, 437 (2018) 410–417. https://doi.org/10.1016/j.apsusc.2017.08.109
7. K. Kisand, A. Sarapuu, A.-L. Peikolainen, **H. Seemen**, M. Kook, M. Käärik, J. Leis, V. Sammelselg, K. Tammeveski, Oxygen reduction on Fe- and Co-

containing nitrogen-doped nanocarbons, *ChemElectroChem*, 5 (2018) 2002–2009. https://doi.org/10.1002/celc.201800353

8. K. Kalam, **H. Seemen**, M. Mikkor, P. Ritslaid, R. Stern, S. Dueñas, H. Castán, A. Tamm, K. Kukli, Electric and magnetic properties of atomic layer deposited ZrO_2-HfO_2 thin films, *ECS Journal of Solid State Science and Technology*, 7 (2018) 117–122. https://doi.org/10.1149/2.0041809jss
9. K. Kalam, **H. Seemen**, P. Ritslaid, M. Rähn, A. Tamm, K. Kukli, A. Kasikov, J. Link, R. Stern, S. Dueñas, H. Castán, H. García, Atomic layer deposition and properties of ZrO_2/Fe_2O_3 thin films, *Beilstein Journal of Nanotechnology*, 9 (2018) 119–128. https://doi.org/10.3762/bjnano.9.14
10. A. Tamm, U. Joost, M. Mikkor, K. Kalam, H. Mändar, **H. Seemen**, J. Link, R. Stern, H. Castan, S. Duenas, K. Kukli, Properties of zirconium oxide and cobalt ferrite layered nanocomposite, *ECS Journal of Solid State Science and Technology*, 6 (2017) P886–P892. https://doi.org/10.1149/2.0331712jss
11. M. Kodu, A. Berholts, T. Kahro, M. Kook, P. Ritslaid, **H. Seemen**, T. Avarmaa, H. Alles, R. Jaaniso, Graphene functionalised by laser-ablated V_2O_5 for a highly sensitive NH_3 sensor, *Beilstein Journal of Nanotechnology*, 8 (2017) 571–578. https://doi.org/10.3762/bjnano.8.61
12. K. Piip, H. van der Meiden, K. Bõstrov, L. Hämarik, J. Karhunen, M. Aints, M. Laan, P. Paris, **H. Seemen**, A. Hakola, S. Brezinsek, Loading of deuterium and helium by Pilot-PSI plasma and their detection by in-situ LIBS, *Nuclear Materials and Energy*, 12 (2017) 694–698. https://doi.org/10.1016/j.nme.2016.12.034
13. A. Tamm, I. Oja Acik, T. Arroval, A. Kasikov, **H. Seemen**, M. Marandi, M. Krunks, A. Mere, K. Kukli, J. Aarik, Plasmon resonance effect caused by gold nanoparticles formed on titanium oxide films, *Thin Solid Films*, 616 (2016) 449–455. https://doi.org/10.1016/j.tsf.2016.08.059

LIST OF ABBREVIATIONS AND SYMBOLS

3D	three-dimensional
ALD	atomic layer deposition
E_c	coercivity (electric)
CCD	charged-coupled device
CVD	chemical vapor deposition
DRAM	dynamic random access memory
EDX	energy-dispersive X-ray spectroscopy
FIB	focused ion beam
GIS	gas injection system
GIXRD	grazing incidence X-ray diffraction
H_C	coercivity (magnetic)
HAADF	high-angle annular dark-field
HRS	high resistance state
HRTEM	high-resolution transmission electron microscopy
LRS	low resistance state
M_s	saturation magnetization
MIM	metal-insulator-metal
MOSFET	metal-oxide-semiconductor field-effect transistor
OLED	organic light-emitting diode
P_r	remnant polarization
PPMS	physical property measurement system
SDD	silicon drift detector
SEM	scanning electron microscopy
STEM	scanning transmission electron microscopy
TEM	transmission electron microscopy
VSM	vibrating sample magnetometer
WDS	wave-dispersive X-ray spectroscopy
XRD	X-ray diffraction
XRF	X-ray fluorescence

INTRODUCTION

The constant development of materials and technology has led to smaller devices in size but higher in functionality. This development, including miniaturization and improvement, is ongoing. There remains a constant demand for new novel materials or material combinations with new or improved functionalities for existing and new applications.

Over the past few decades, the development of multilayer thin films has been of great interest due to their fundamental properties and use in diverse technological applications [1]. The multilayer thin films have a unique geometry, with layer thicknesses on the nanoscale (below 100 nm), causing them to have a wide range of unique and novel properties not observed in bulk material [1]. Multilayer thin films can be grown by combining many different materials while having high control over thickness and composition. The properties of multilayer thin films are, among other things, affected by thicknesses and the type of materials used for the constituent layers [1]. These are some of the reasons why multilayer thin films are and will continue to be widely applied in nanotechnology.

After the continuous evolution and successful scaling, the non-volatile flash memory and other charge-based memories are approaching their miniaturization limit due to physical limitations [2–6]. Furthermore, flash memories have some disadvantages, such as high writing voltage, low operation speed and poor endurance [4]. One way to overcome this problem and continue scaling further is to switch from charge-storage based memory to a non-charge-storage based memory [2, 5]. For example, to use resistance change as the property to store the information instead of charge storage [5]. A promising candidate for the next-generation non-volatile memory has been claimed to be a resistive switching random access memory due to its high speed and efficiency, great reliability, energy-saving characteristics, and excellent scaling capability [2–6]. Resistive random access memory is based on the resistive switching phenomenon, which is a sudden non-volatile and reversible change in the material's resistance under the influence of external electrical stimuli. Such materials showing the resistive switching effect are, for example, insulating or semiconducting (transition) metal oxides [2, 3]. A resistive random access memory cell comprises insulating or semiconducting materials sandwiched between two metal electrodes [3, 4]. It operates on the principle that the resistance between the two electrodes can be altered by applying voltage on (or forcing current through) the device [5].

Another actively researched field for novel multifunctional materials is the field of multiferroics and magnetoelectrics [7]. Multiferroics are materials in which at least two out of three "ferroic" types are present [8]. These three phenomena are ferroelectricity, ferromagnetism, and ferroelasticity [8]. The beneficial interest in multiferroic materials is related to the possibility of strong magnetoelectric coupling [8]. These materials are attractive because there is a possibility that the electric field not only reorients the electric polarization but also controls the magnetic polarization, and the magnetic field can change the electric polarization [8]. Multiferroics are attractive materials for novel memories [7, 9], magnetoelectric sensor materials [7, 9] and actuators [10], provided that these properties are present at room temperature in materials with thicknesses in nanoscale. However, the coexistence of ferromagnetism and ferroelectricity in the material is rare but not impossible [7, 8]. There are very few materials with multiferroic properties, especially in a thin film form. Still, those that have tend to have significantly enhanced multiferroic properties compared to bulk materials [7, 10].

The difficulties with the processes resulting in reliably performing multiferroic thin films are somewhat related to the commonly observed appearance of multiferroic and magnetoelectric behaviour in ternary, quaternary or even more complex compounds, which are, at the same time, to be formed in well-ordered and chemically pure lattices. These demands essentially reduce the robustness and reproducibility of the deposition process, which otherwise are the prerequisites for producing device-compatible material layers, especially on large technologically relevant substrate areas and three-dimensional substrate structures.

Different horizontal multilayer heterostructures as well as single-phase layers, i.e. thin film multiferroics, have been of interest, presumably providing coupling between ferroelectricity and antiferromagnetism [11–13]. Regarding single-phase materials, perovskite oxides, such as $BiFeO_3$ [7, 10, 11], $BiMnO_3$ [14] and $SmMnO_3$ [15] deposited by sputtering or laser ablation, have been considered as compounds able to perform as magnetoelectric layered solids. In the case of multilayer heterostructures, it seems that, in some cases, the structures expected to behave as promising multiferroics consisted of ferroelectrically and/or magnetically polarizing complex oxides and ferromagnetic metal layers. For instance, resonant ferroelectric and ferromagnetic switchings have been monitored in stacks consisting of ferromagnetic metal alloys or oxides, and ferroelectric perovskite oxide, as realized by NiFe layers sputtered on chemical solution deposited ferroelectric $Pb_{0.92}La_{0.08}Zr_{0.52}Ti_{0.48}O_3$ films [16], $(Pd/Co)_3$ deposited on a monocrystalline Cr_2O_3 [12], or laser-ablated ferromagnetic $CuFe_2O_4$ layers on sol-gel deposited ferroelectric $Pb(Zr_{0.52}, Ti_{0.48})O_3$ films [17]. Creating the multiferroic materials artificially by combining ferromagnetic and ferroelectric materials into multilayers has been recognized as a promising research focus in the field of multiferroics [7].

Few works have so far been devoted to materials with abilities to polarize nonlinearly and saturatively in both magnetic and electric fields and, in addition, exhibit resistive switching characteristics. Saturative magnetization has been influenced by electrical resistivity switchable in HfO_2/Nb:$SrTiO_3$ stacks, where HfO_2 films were laser ablated onto monocrystalline $SrTiO_3$ substrates [18]. Resistive switching has independently been recorded in laser-ablated ferromagnetic $La_{2/3}Ca_{1/3}MnO_3$ films [19]. Multiferroic behaviour was investigated for double layers of oxides consisting of $Bi_{0.8}Pr_{0.2}Fe_{0.95}Mn_{0.05}O_3/Bi_{3.96}Gd_{0.04}Ti_{2.95}W_{0.05}O_{12}$ stacks deposited by sol-gel technique [20] and also in $La_{0.5}Pr_{0.5}FeO_3$ films obtained in a dip-coating process using a polymeric organic solution [21]. Ferroelectric, ferromagnetic and resistive switching abilities were all targeted in these latter structures, although coupling between all the mentioned properties was not registered.

One can notice that the materials, which have tended to behave as multiferroics, also appear often rather complex in terms of their stoichiometry. Synthesis of such compounds and deposition of thin films with similar multinary composition on large area wafer substrates, in accord with the demands for current nanoelectronics, can be expectedly overwhelmingly complicated. Moreover, the films with defined crystal structure and uniform chemical composition must be grown on three-dimensional substrate structures to thicknesses in the range of few (tens of) nanometers for today's applications. For this reason, it would be highly desirable if one could find solid materials of essentially simpler stoichiometry, in particular, binary compounds (e.g. HfO_2, ZrO_2, Fe_2O_3), stabilized in phases exhibiting advanced electrical and/or magnetic properties. The deposition and processing of advanced functional materials would then become more convenient and feasible on large-area 3D substrates, as required. In addition, in the multilayer (i.e. superlattice-like) structures, different physical properties (for example, electrical or magnetic polarizabilities or variable conductivity) of constituent binary compounds could be usefully tailored while maintaining structural and compositional uniformity in wafer scale.

Understanding the material's behaviour at the atomic level and linking it with properties can help build better products and shorten the development time. Along with the development of technology and miniaturization of novel devices, the importance of precise and advanced characterization tools, including microscopical devices, has also emerged. Electron microscopy is a complementary branch to nanotechnology for advanced and precise analysis of different material types [22]. The most comprehensive techniques for advanced study of materials are considered transmission electron microscopy, scanning electron microscopy, focused ion beams, and atomic force microscopy [22]. Microscopy can, for example, in combination with spectroscopy, provide information about material characteristics, size, thickness, morphology, crystallinity and elemental composition in scales going down to single atoms. In addition, the possibility of creating cross-sections of the samples using the focused ion beam technique and imaging this cross-section with transmission electron microscopy is a powerful tool for investigating multilayer thin films. Studying cross-sections is valuable because, among other things, it provides information about whether the deposited layers are mixed and the thicknesses of the layers.

The purpose of this study was to contribute to the search and characterization of new and novel material combinations that would show ferromagnetic, ferroelectric and/or resistive switching behaviour at room temperature, which are attractive properties for novel memory devices. The aim was to combine potentially ferromagnetic and ferroelectric materials (mainly metal oxides) into multilayer structures (nanolaminates) and mixed films. It was speculated that the attractive properties of the different metal oxides would also remain present in nanolaminates. There may be additional beneficial effects present at the interfaces of the layers or thanks to multilayer structure. It was also acknowledged beforehand that overcoming the challenges in stabilizing specific metastable phases of the material might enhance the material's behaviour due to the specific nature of this phase and the correspondingly increased amount of defects. One example is the rare and metastable orthorhombic ε-Fe_2O_3 phase, which is known for its unusually high coercivity and multiferroic properties [23–25]. One example from the ferroelectric materials point of view is a metastable orthorhombic HfO_2 phase previously acknowledged for its ferroelectric properties [26–30].

The atomic layer deposition (ALD) method was selected to fabricate thin films and nanolaminates due to its ability to provide high-quality thin films and precise thickness control over large substrate areas through alternate self-limiting surface reactions [31–33]. Besides, ALD has already proven itself a suitable and widely used method in many research and industrial applications [32–39], including the field of microelectronics [32, 33, 37].

In the present Thesis, the ALD multilayer structures studied were Fe_2O_3-BiOCl composites [**I**], Er_2O_3-Fe_2O_3 mixed thin-film structures [**II**], ZrO_2-Co_3O_4 nanolaminates [**III**], ZrO_2-Al_2O_3 and HfO_2-Al_2O_3 mixed films and nanolaminates [**IV**, **V**]. The characterization of the deposited films mainly focused on examining the phase composition, investigating surface morphology and/or cross-sections, and studying the samples' magnetic and electrical behaviour. In the latter case, the samples' polarisation characteristics in the presence of an external magnetic or electric field were determined, and resistive switching behaviour was studied. Complementarily, cross-sections of the selected films deposited on high aspect ratio three-dimensional (3D) substrates were studied to examine the thin film growth's conformality to these substrates.

THE CLAIM OF THE THESIS

The author of this Thesis claims that the atomic layer deposition method can be used to create such mixed thin films and nanolaminates that show ferromagnetic, ferroelectric and resistive switching behaviour at room temperature. Further, under certain deposition conditions, it is possible to stabilize metastable phases in multilayer structures, improving their magnetic and electrical properties. In addition, electron microscopy (both scanning and transmission electron microscopy) is necessary and valuable to characterize nanolaminate structures' quality and carry out research on an adequate level.

Five original and published scientific papers (denoted **I**–**V**) are presented to justify and discuss the claim.

ATOMIC LAYER DEPOSITION

Atomic layer deposition (ALD) is a gas-phase chemical deposition method and a thin film deposition technique based on the sequential use of self-terminating gas-solid reactions [31, 32, 40]. Self-terminating means that these reactions continue until there are suitable reactive sites available on the substrates, after which the reactions will naturally stop [31]. ALD precursors can be gases, volatile liquids, or solids [41], and there can be two or more precursors used for the deposition. The precursor's vapour pressure should be high enough for feasible evaporation and effective mass transportation [41], and all solid and some liquid precursors need to be heated [41]. Sequential use of gas-solid reactions in the ALD context means that the precursor gases and vapours are alternately pulsed into the reaction chamber and onto the substrate surface, where subsequent chemisorption or surface reaction steps of the precursors take place [42, 43]. The separation of precursor pulses is required in ALD to avoid the precursors' simultaneous presence in the gas phase and consequent uncontrolled chemical vapour deposition (CVD) growth [31].

One ALD cycle consists of four characteristic steps, also known as pulses (Figure 1):

1. The first precursor pulse – The first precursor A (e.g. $ZrCl_4$) is transported into the reaction chamber, where it reacts in a self-limiting manner with the available functional groups on the surface covered with hydroxyls.
2. Purge – The unreacted precursor A molecules (e.g. $ZrCl_4$) and the reaction by-products (e.g. HCl) are purged from the reaction chamber by an inert carrier gas (N_2).
3. The second precursor pulse – The second precursor B (e.g. H_2O) reacts in a self-limiting manner with the first precursor's surface species.
4. Purge – The unreacted precursor B (e.g. H_2O) and the reaction by-products (e.g. HCl) are purged from the reaction chamber by an inert carrier gas (N_2).

This four-step ALD cycle is repeated as many times as needed until the thin film's desired thickness is achieved. By the end of one completed ALD cycle, up to one monolayer of film material can be deposited on the substrate. Even though the growth is usually less than one monolayer of film material per cycle, the growth of one full monolayer per cycle might be possible when small molecules and elements are used as precursors [41]. As the thin film is deposited layer-by-layer, the film's thickness can be tailored by the number of ALD cycles [32]. Such thickness control of the deposited thin films at the subnanometer level is considered one of the advantages of the ALD process [31, 32].

Thanks to its operation principle based on separate, sequential and self-terminating reactions dependent on the substrate's receiving capability, ALD can provide conformity, allowing uniform coverage of complicated and deep cavities and high aspect ratio 3D structures [31, 32, 40, 44]. Other advantages of ALD are low deposition temperatures [31, 41], tunable film composition [32], control of the stoichiometry of the films [31], pinhole-freeness [31, 34] and high density of the films [31], and convenient process control [31]. ALD can also be used for depositing mixed thin films and different multilayer structures [42, 45].

These advantages have made ALD emerge as a powerful tool for many research and industrial applications [32–39]. Some examples are optoelectronic devices, including thin film electroluminescent displays [33, 34, 37] and organic light-emitting diode (OLED) panels [34, 37, 46, 47]; microelectronics, including metal-oxide-semiconductor field-effect transistors (MOSFETs) [32, 33, 37], dynamic random access memories (DRAMs) [32, 33, 37] and hard disk drive magnetic heads [33]; different protective coatings, including anti-tarnishing coatings on jewellery [33] and anti-corrosion coatings [36, 48–50]; optical coatings [51]; and several medical and biological fields related applications, such as biosensors [38, 39], coatings for medical imaging instruments [38] and bio-compatible coatings for medical implants [38].

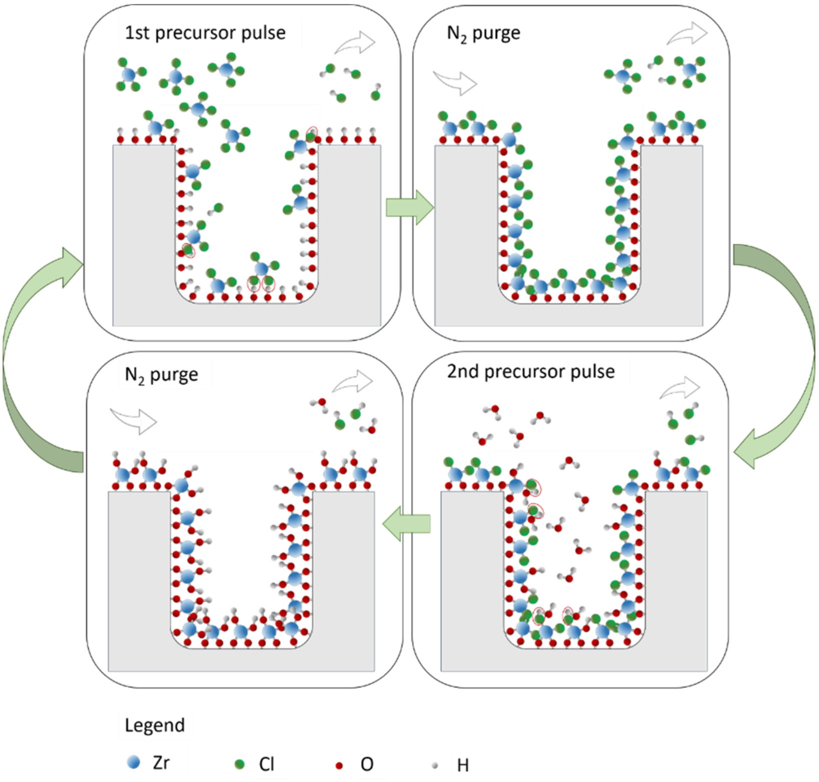

Figure 1. Schematic representation of one ALD cycle (inspired by [52]) of the ZrO_2 thin film deposition process using $ZrCl_4$ as the 1st precursor and H_2O as the 2nd precursor. Legend contains colour codes of the elements used. Grey shape indicates 3D substrate. Red ovals schematically indicate reaction sites, where the by-product HCl forms as a result of the reaction. Displayed atomic radii are not scaled to real radii of the corresponding atoms. The white arrow indicates the carrier gas flow direction; inert carrier gas molecules (N_2) are not separately displayed on this scheme.

SCANNING ELECTRON MICROSCOPY

A scanning electron microscope (SEM) is an instrument that provides images of the sample's surface by scanning it with a focused beam of electrons (electron beam) [53]. It creates magnified images that can provide microscopic-scale information on the surface topography, size, shape, composition, crystallography, and other specimen properties [54, 55]. In principle, a finely focused beam of energetic electrons is created and accelerated to high energy, typically up to 30 keV [55]. The electron beam is then modified by apertures, magnetic and/or electrostatic lenses, and electromagnetic coils that reduce the beam diameter and scan the beam focused on the sample's surface in a raster (x–y) pattern [55]. The interaction between the electron beam and solid material occurs. The intensity of the resulting specific type of electron signals (discussed below) is measured at each beam location on the sample, converted, and subsequently used to obtain an image [55].

The interactions between an electron beam and solid material can produce backscattered electrons, secondary electrons, characteristic X-rays, Auger electrons, and cathodoluminescence [56]. The electron beam's penetration depth and penetration shape depend on the acceleration energy of the electron beam and the atomic number of the elements present in the specimen [56]. The penetration depth can be up to ~2 μm [56]. Characteristic X-rays can be used for collecting information about the elemental composition if the SEM device is equipped with wave- or energy-dispersive X-ray spectroscopy (WDS or EDX) equipment [53]. The two main types of electron signals detected and used for obtaining an image are secondary electrons and backscattered electrons [55–57].

The secondary electrons are emitted from the specimen when the interaction with the primary beam causes the ionization of specimen atoms [54–56]. They escape the sample with very low kinetic energies – less than 50 eV, typically around 3–5 eV, and, therefore, they only escape from a region within a few nanometers of the surface [54–56]. As a result, secondary electrons provide topographic information with good resolution [54, 56].

Backscattered electrons are electrons from the primary electron beam that have undergone a single or multiple scattering events and escape from the surface with remaining energy higher than 50 eV [56]. Backscattered electrons can provide both compositional and topographic information [56]. However, due to higher energy and a considerably deeper and larger region from which backscattered electrons are produced, the lateral resolution is not as high compared to the secondary electrons [54, 56]. The backscattered electrons can provide valuable compositional information in the form of atomic number contrast [54, 56]. Elements of higher atomic numbers appear brighter because they have more positive charges on the nucleus, which means that more electrons are backscattered, causing the resulting backscattered signal to be higher [54, 56].

In the current study, SEM was mainly used to investigate the surface morphology and cross-sections of the selected samples. It was also used to assist the specimen preparation process for transmission electron microscopy discussed in the next chapter. In combination with EDX equipment, the elemental composition of the selected samples was also studied.

FOCUSED ION BEAM TECHNOLOGY AND DUAL-BEAM DEVICES

The focused ion beam (FIB) technology is a versatile tool that can be used for imaging and modifying the samples through ion milling/etching and beam induced deposition [22]. In principle, FIB is somewhat similar to SEM, but in FIB, instead of an electron beam, the focused ion beam, for example, a few nanometers wide Ga^+ ion beam, is generated and directed to the sample surface. This ion beam is moved point-by-point and line-by-line across the object's surface, and the resulting interactions between the ion beam and target materials also differ a bit compared to SEM [56]. These interactions between ion and solid material produce secondary ions, secondary electrons, X-rays, back-sputtered ions, neutral atoms, and clusters from target materials [56]. The penetration depth of the ion beam is about 10–20 nm, which is less compared to the electron beam [56]. An ion beam with a lower beam current is used for imaging, and secondary ions or secondary electrons are detected to obtain an image of the object. An ion beam with a higher beam current is used to remove material from a specific desired area as such interaction with FIB is destructive to the specimen.

Initially, the FIB devices were attractive for their unique capabilities for circuit modification and computer chip repair in semiconductor technology [22, 58, 59]. Over time and with the introduction of dual-beam devices, consisting of SEM and FIB columns and additional equipment such as gas-injection systems, nanomanipulators and chemical analysis tools, the application range of these devices has significantly increased [22, 59]. Some of the applications of dual-beam devices are microelectronic failure analysis, site-specific cross-sectioning of challenging materials/samples and device modification/editing [59]. Preparing samples (also known as lamellae) for transmission electron microscopy is considered one of the most important and commonly used FIB related applications of dual-beam instruments [22, 58]. It has also been considered the best technique for site-specific transmission electron microscope (TEM) specimen preparation, especially when hard materials or substrates are involved [22, 58]. There is no other technique for TEM specimen preparation that would allow such a precise selection of the target area [58]. It is also reliable and considered fast compared to other preparation techniques [22, 58]. It is also suitable for almost any type of material (hard or soft or a combination of both) [22, 58]. Creating TEM specimens, i.e. lamellae, that are ultrathin and electron-transparent is possible thanks to the controlled ion milling abilities of the device [22]. The main disadvantage of using FIB is the possibility of the formation of FIB induced damaged layer due to gallium implantation, redeposition of sputtered particles and amorphization of the material [22, 58]. The deposition of protective layers and the use of lower ion beam currents during polishing steps help minimize the redeposition and amorphization effects [22].

There are mainly two types of TEM sample preparation techniques by FIB: the methods that require prethinning of the sample by other tools and the "lift-out" type of methods [58, 60]. In situ lift-out type lamella creation technique is considered the most common way for TEM specimen preparation [22]. In this technique, a small piece of sample is extracted from a specific site and transferred to a TEM half grid, where the final milling/polishing is performed [22, 58]. This technique requires a device equipped with a manipulator unit to move the piece of sample to the TEM grid [22]. It also involves using an ion beam-assisted platinum deposition for attaching the lamella first to the manipulator and later to the TEM grid [22]. This lamella creation technique was also the technique used in the current Thesis, and the process is discussed in more detail in the experimental section.

(SCANNING) TRANSMISSION ELECTRON MICROSCOPY

Transmission electron microscopy (TEM) is a microscopy technique in which a beam of electrons is transmitted through a specimen, and the resulting interactions between the sample and beam of electrons generate specific signals that are used to form an image and gather valuable information [61, 62]. The interaction between the specimen and beam of electrons result in transmitted electrons, backscattered electrons, secondary electrons, Auger electrons, visible light, X-rays (characteristic and continuum) and heat [62]. Transmitted electrons include unscattered, elastically scattered and inelastically scattered electrons. Elastically scattered electrons did not lose energy while scattering, while inelastically scattered electrons did [62]. All three types of transmitted electrons contain valuable information for electron diffraction and imaging [62]. The characteristic X-rays can, similarly to SEM, be used for elemental mapping and collecting information about the chemical composition if the TEM device is equipped with suitable spectroscopy equipment and also has scanning transmission electron microscopy (STEM) capabilities [62]. While in a traditional TEM, the electron beam illuminates the specimen uniformly, STEM is a modification of the traditional TEM technique in which a nanometer-sized beam of electrons is scanned point by point across the specimen [1].

Modern S/TEM devices provide a range of different imaging modes that use various image contrast mechanisms, such as mass-thickness contrast imaging, diffraction-contrast imaging, Z-contrast imaging in STEM, and a phase-contrast in high-resolution TEM (HRTEM) [62]. The Z-contrast images are also known as high-angle annular dark-field (HAADF) images [1]. The HAADF images are formed from the electrons incoherently scattered at very high angles (>50 mrad), collected with the high-angle annular dark-field detector [1]. The HAADF images are sometimes called Z-contrast images because they contain intensity proportional to the square of the atomic number (Z) of the scattering atom while lacking diffraction contrast and having minimal if any phase contrast [1].

The detectors and resulting images can also be divided into the bright field and dark field detectors and images. A bright-field detector includes the transmitted (unscattered) beam while scattered electrons are blocked, which means that the holes or regions beyond the specimen edge appear bright, whereas the areas that absorb or scatter electrons, including crystalline or high mass materials, appear darker [56, 57]. A dark-field detector excludes the transmitted (unscattered) beam and collects only the scattered electrons, which means that the areas with no electron scattering, for example, holes and areas containing no specimen, appear dark, while regions with material appear bright [56, 57].

Understandably, detecting transmitted electrons means that the samples must be thin enough to become transparent to electrons, often requiring time-consuming, destructive, and more complex specimen preparation techniques than SEM [54, 62]. The area of interest should be typically less than 100 nm thick to be transparent to electrons [62], which is why lamellae are prepared from deposited multilayer structures before TEM measurements can be performed. One of the TEM advantages is its resolution up to angstrom level [62]. In the current study, the STEM/TEM was mainly used to characterize the cross-sections of the nanolaminate structures by studying the lamellae cut out from the samples. In combination with energy-dispersive X-ray spectroscopy equipment, the composition profiling of the nanolaminates was studied.

EXPERIMENTAL METHODS

Deposition and formation of the thin film structures

The ALD experiments were carried out using a flow-type in-house built hot-wall ALD reactor [63] [**I–III**] or a commercial flow-type hot-wall reactor F120 [64] (ASM Microchemistry, Ltd.) [**IV**, **V**]. A flow-type reactor means that reactants are transported to the substrates located in a reaction chamber by an inert carrier gas, which flows through the reactor in a viscous flow regime [52]. N_2 was used as this carrier and purging gas in the case of all deposition experiments. In all cases, a single ALD cycle was started with a metal precursor pulse and continued with a purge of the reaction zone with the pure carrier gas, oxygen precursor pulse and another purge of the reaction zone. The majority of the metal precursors used were various chlorides ($FeCl_3$ [**I**], $BiCl_3$ [**I**], $ZrCl_4$ [**III, IV**], $AlCl_3$ [**IV, V**], $HfCl_4$ [**V**]) with some exceptions ($Er(thd)_3$ [**II**], $FeCp_2$ [**II**], $Co(acac)_3$ [**III**]). Oxygen precursors used were H_2O [**I, IV, V**] and O_3 [**II, III**]. In the case of $Er(thd)_3$ [**II**] and $Co(acac)_3$ [**III**] metal precursors, using ozone as an oxygen precursor was necessary as these metal precursors do not react well with the H_2O. Water is a commonly used oxygen precursor, but in some cases, it is useful to prefer ozone to reduce the number of residual hydrogen impurities in a thin film. Residual hydrogen combined with residual chloride (originating from metal chloride precursors) can provoke HCl formation. Ozone has also attracted increasing interest as the oxygen source due to its generally higher oxidation potential compared to H_2O at a normal ALD temperature range, especially when the ALD process temperature approaches the upper limit of the ALD temperature window [65]. Moreover, in the case of diketonate and acetylacetonate-type metal precursors, the reactivity of water is often not sufficient to effectively exchange thd- and acac-ligands and initiate the growth of metal oxide films with an appreciable rate. In such cases, distilled water, otherwise possibly the most common oxygen precursor in ALD, has to be replaced by ozone. Deposited structures ranged from one [**I–V**] or two-layer structures [**I**] to mixed films [**II, IV, V**] and nanolaminates [**III, IV, V**]. An overview of the deposited structures is presented in Table I. Complete information about the critical deposition related parameters, including precursor evaporation and deposition temperatures, pulse lengths and the number of deposition cycles, is available in the original publications [**I–V**].

For the same deposition process, several different types of substrates can be added to the reaction chamber. One way to select the substrates is to make a decision based on the desired properties to be tested and the expected field of application. In this Thesis, the primary substrates were pieces of undoped Si(100) [**I**, **III**] or undoped Si(100) wafers covered with a 1.5–2.0 nm thick wet-chemically-grown SiO_2 [**IV, V**], highly doped Si(100) covered by 5 or 10 nm thick TiN layer [**I–V**], and three-dimensional (3D) substrates [**I**, **II**]. Silicon substrate is the primary substrate used in the field of electronics. Undoped silicon substrates were preferred for different characterization activities, including magnetometry studies. These substrates help avoid possible interferences by magnetization signal and noise from the substrates [**II**]. Highly doped conductive silicon wafer pieces covered by TiN layer were mainly used as bottom electrodes for electrical measurements. The 3D substrates, i.e. Si substrates having a regular pattern of vertical etched channels (Figure 2, 3), were used to investigate the ability of the deposited film to follow the shape of the 3D substrate. Higher step coverage, i.e. the ratio of film thickness on the bottom of the channel to that on the top [66], is desired when there is a need to coat arbitrarily shaped nano-structures with the functional films [67]. Two types of 3D substrates were applied in the studies on the examination of the conformality of metal oxide film growth – trenches with the 60:1 aspect ratio [**I**] (Figures 2 and 3) and stacks with the 20:1 aspect ratio [**II**]. The aspect ratio here indicates the ratio between the height and the width of the 3D substrate. For additional information about the substrates and pre-treatments, refer to original publications [**I**–**V**].

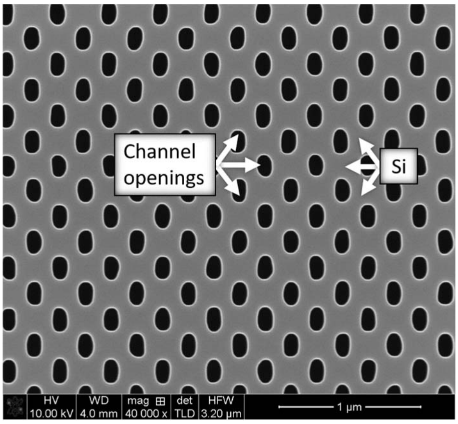

Figure 2. Bird-eye view SEM image of the empty trench type 3D substrate (prior depositions). Labelled arrows point to the silicon substrate and the openings of the channels (trenches) inside it.

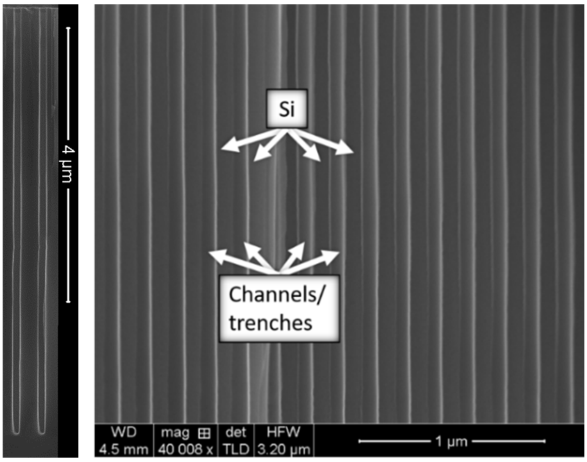

Figure 3. Cross-sectional SEM images of two empty trenches at their full length (left panel) and the middle part of the channels (right panel) before depositions. Labelled arrows point to the trenches (channels) and the silicon between them.

Table I. An overview of the types of deposited structures.

Study no.	Deposited oxide A	Deposited component B	Combinations	Description
I	Fe_2O_3	BiOCl	A + B; A & B	Seven two-component structures (thin-film as a bottom layer and nano-flakes on top) deposited using a variation of the number of ALD cycles; Reference thin films
II	Er_2O_3	Fe_2O_3	N × (A + B) (N=500, 200, 22, 20); 2 × (A + B) + A A & B	Six mixed thin-film structures with different cycle ratios Reference thin films
III	ZrO_2	Co_3O_4	2 × (A + B) + A; 2 × (B + A) + B; A & B	5-layer nanolaminates deposited using a fixed number of ALD cycles per layer (A=100, B=200); Reference thin films
IV	ZrO_2	Al_2O_3	5 × (A + B) + A; 3 × (A + B) + A; 6 × (A + B) + A; A	Mixed films and nano-laminates deposited using a variation of ALD cycle ratios and number of layers; Reference thin film
V	HfO_2	Al_2O_3	N × (A + B) + A (N = 2..6, 11, 31, 33..35); A	14 mixed films or nano-laminates deposited using a variation of ALD cycle ratios and number of layers; Reference thin film

Post-deposition annealing of the samples may result in changes in phase composition, for example, change of the phase [68–72] and rate of the crystallographic ordering [68, 70, 71], and transformation from amorphous to crystalline [70, 73–75]. Annealing can also induce mixing of layers or interfaces [73, 75] or formation of new interfaces [70, 74, 75], reduction of the residual elements or compounds inside the thin film (for example, residual hydrogen) and related defects [70, 72, 75]. An increase [74, 76] or decrease [77] of the concentration of vacancies, such as oxygen vacancies, has also taken place as a result of post-deposition annealing, depending on whether the annealing procedure was conducted in either reducing or oxidizing environments. Properties of the material are often also directly connected with the phase composition. Therefore, to investigate the heat-treatment effect on the film crystal structure and properties, some of the deposited thin-film structures were annealed after deposition in air ambient [**I, IV, V**].

Characterization of thin-film structures

A wavelength-dispersive X-ray fluorescence (XRF) spectrometer Rigaku ZSX400 with the ZSX software was used to evaluate the elemental composition and mass thickness of the samples [**I–III**]. Mass thickness can be used to estimate the thickness of the film if the density of the material is known. The crystal structure of the samples in the case of all studies was evaluated by using the grazing incidence X-ray diffractometry (GIXRD) method. Grazing incidence X-ray diffraction patterns were recorded by Smartlab (Rigaku) X-ray analyzer using Cu Kα radiation [**I–III**] or with PANalytical X'pert Pro MPD diffractometer [**IV**, **V**]. Cu Kα radiation corresponds to an X-ray wavelength of 0.15406 nm. The same Rigaku equipment was also used for X-ray reflectometry (XRR) studies which were performed to estimate the densities and thicknesses of the films [**II**]. In one study, the thicknesses of the films [**III**] were partly determined using GES5E spectroscopic ellipsometer by Sopra-Semilab. In the same study, the time-of-flight elastic recoil detection analysis (ToF-ERDA) was used for evaluating the composition profile of the samples [**III**], including the detection and determination of the content of light residues such as hydrogen, carbon and nitrogen. For more information, refer to original publications [**I–V**].

Two different scanning electron microscopes (SEM) were used to study the chosen samples. These devices were Hitachi S-4800 scanning electron microscope equipped with an Oxford INCA 350 energy-dispersive X-ray (EDX) spectrometer and FEI Helios Nanolab 600 DualBeam scanning electron microscope equipped with a focused ion beam module (SEM-FIB), gas injection system (GIS), Omniprobe model 100.7 in-situ nanomanipulator, scanning transmission electron microscopy (STEM) mode and an INCA Energy 350 EDX spectrometer by Oxford Instruments. Both instruments were used to study the morphology of the samples [**I–IV**] and perform an electron probe microanalysis with EDX module [**I**, **IV**, **V**]. Electron probe microanalysis was mainly used to determine the cation ratio and estimate the film thickness [**IV**, **V**]. Standard SEM specimen mounts with horizontal surface were used for these studies, and commonly used carbon double-sided adhesive discs were used to fix the samples to these specimen mounts.

The Helios SEM-FIB device was also used to investigate the cross-sections of the samples deposited on planar [**I**] or 3D substrates [**I**, **II**]. Even though the FIB module could have easily been used to create more uniform cross-sections of the samples with high precision of the cross-section site's location, cleaving the samples mechanically into half was preferred. It was mainly preferred to avoid the possible negative influence of the FIB on the samples, for example, amorphization [22, 58, 60, 67]. Other reasons listed in our previous study [67] were short cross-section sample preparation time; the possibility of investigating larger areas compared to the regular FIB created cross-sections; a lack of need to deposit a protective (Pt) layer to protect the surface against FIB. Hence, mechanical cleaving is faster, cheaper and the captures of the cross-sections are sharper. Some of the disadvantages of mechanical cleaving were lower control over the breakage/ cross-section area's location and the roughness of the cross-section area due to uncontrollable crack formation. These disadvantages were more apparent while studying the samples deposited on a 3D substrate. It resulted in longer time spent moving along the edge of the broken side to find desired sites where the trenches would be visible in their entirety to capture the cross-sections. These disadvantages did not significantly affect capturing the cross-sections of the thin film samples deposited on planar substrates, thanks to their evenly distributed thin film layers. Carbon double-sided adhesive discs were also used to fix a piece of the cleaved sample to specimen mount for cross-section investigation. In addition to standard SEM specimen mounts with a horizontal surface, another standard specimen mount with a vertical surface was mainly used to investigate the cross-sections. This mount allowed fixing the sample vertically to a substrate, which means that the side of interest was already facing the electron probe for the cross-section investigation.

FEI Helios Nanolab 600 DualBeam SEM-FIB device was also used for creating lamellae of the specimens for transmission electron microscopy (TEM) studies using the in-situ lift-out type lamella creation method [**III**, **IV**, **V**]. The samples were fixed to a regular sample mount beforehand (Figure 4, c) using fast-drying silver paint/paste, to fasten the specimen as firmly as possible for precise lamella preparation operation. This conductive silver paste consists of very fine flake silver suspended in iso-butyl methyl ketone. Omniprobe 3 post copper lift-out type (TEM) grids were attached to a standard TEM grid mount (Figure 4, a) and holder (Figure 4, b) specified for this procedure. After that, the standard set-up of required holders and accessories needed for this procedure was set up and fixed to the specimen chamber, as shown in Figure 4. The chamber door was closed, and the specimen chamber vacuum was restored. Regular adjustments in the settings were made, the site of which lamella would be cut out was selected, and the eucentric position was set. In order to protect the area of interest during the lamella creation process, small (~20×1 μm) and thin (~1 μm) rectangular shaped C and Pt layers were deposited on top of the sample using the gas injection system and the help of electron beam (for the first C and Pt layers) or Ga^+ ion beam (the last Pt layer) (Figure 6, a). The sample was tilted from 0° to a 52° angle for the deposition of the last Pt layer (Figure 5). Tilting to a 52° angle is necessary due to the placement of SEM-FIB columns in the dual-beam device – to deposit a Pt layer with the help of an ion beam, the surface of the sample should be facing in the direction of the ion beam. The gas compounds, which were naphthalene [$C_{10}H_8$] for C deposition and methylcyclopentadienyl trimethyl platinum [$(CH_3)_3Pt(C_pCH_3)$] for Pt deposition, were directed onto the target specimen through the gas injection nozzle and adsorbed on the specimen's surface. This was followed by a bombardment of adsorbed molecules with a focused beam within predefined patterns.

Lamella creation process started with milling the trenches to both sides of the Pt stripe using the ion beam with the maximum beam current (21 nA) (Figure 6, a) followed by extending the trenches up until the Pt stripe using the ion beam with the reduced beam current of 9.3 nA (Figure 6, b). After that, two and a half sides of lamella were detached from the specimen by milling (Figure 6, c). The sample was tilted back to 0°, and the beam current was reduced to at least 0.46 nA before that.

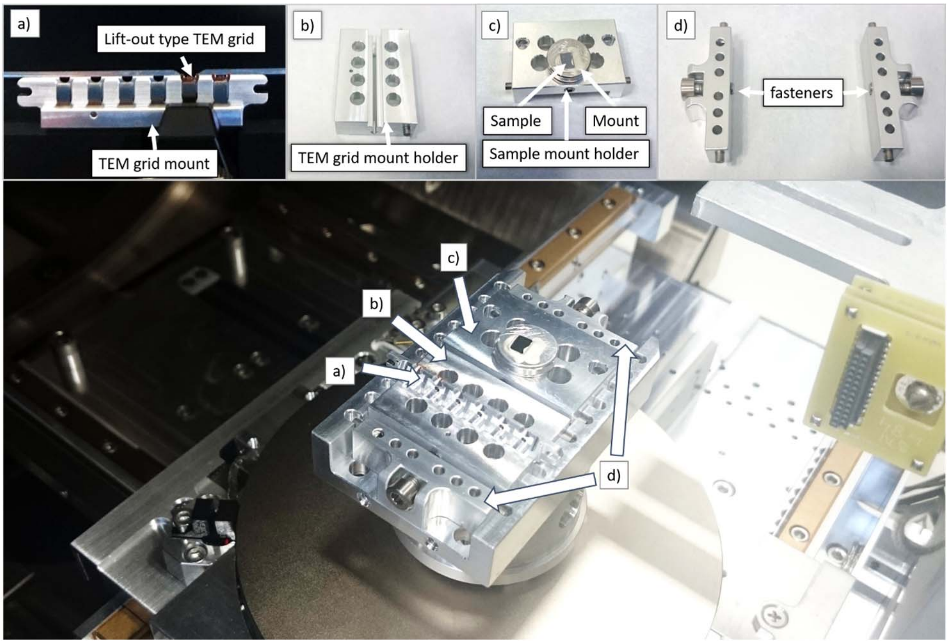

Figure 4. The standard set-up of required holders and accessories needed for lamella creation. Lift-out type TEM grid attached to a TEM grid mount (a), which is, in turn, placed into a TEM grid mount holder (b). Sample attached to the sample mount, which is, in turn, put into the sample mount holder (c). Both mount holders and outmost details (d) are placed into designated slots and fixed with fasteners.

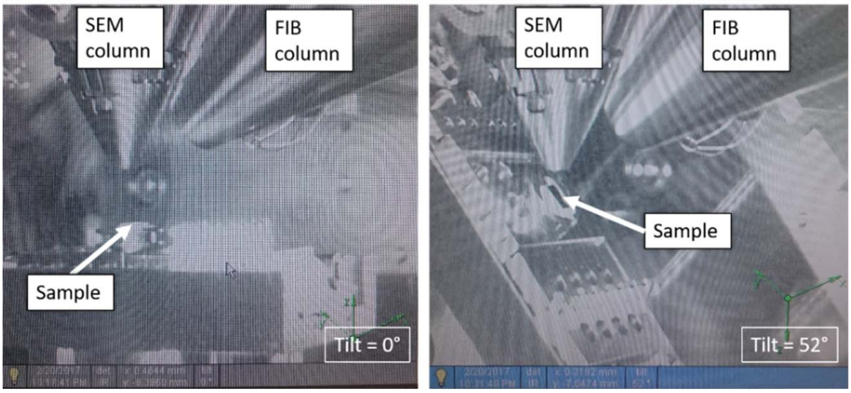

Figure 5. Images of the charged-coupled device (CCD) camera images of the view of the specimen chamber. On the left panel, the untilted sample is facing in the direction of the electron-beam column. On the right panel, the sample tilted to a 52° angle is facing the ion-beam column's direction. SEM and FIB columns are marked with labels.

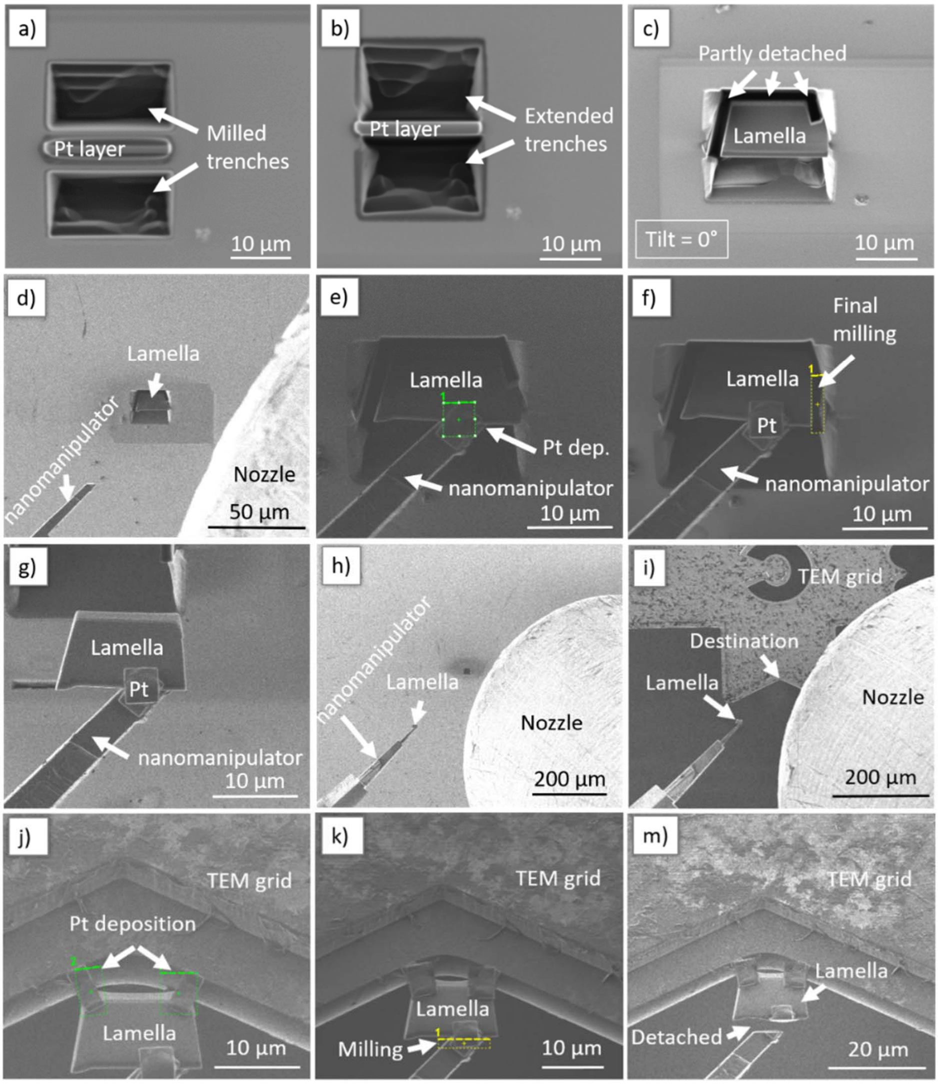

Figure 6. Focused ion beam images of the milling out and transportation steps of the lamella creation process – (a) milling trenches to both sides of the Pt stripe, (b) extending the trenches, (c) detaching two and a half sides of lamella by milling, (d) moving the nanomanipulator closer to the lamella, and (e) into contact with the lamella followed by depositing Pt to the contact surface, (f) performing milling to detach the lamella from the specimen, (g) lifting out the lamella, (h) moving the lamella away from the sample and (i) closer to the TEM grid, (j) depositing Pt to attach lamella to a grid, (k) milling the connection between lamella and nanomanipulator (m) to detach the lamella from nanomanipulator.

Lamella transportation was performed using the model 100.7 in-situ nanomanipulator. The tip of the nanomanipulator was moved closer to the lamella (Figure 6, d) and cleaned. The tip was moved into contact with the lamella's edge, and lamella was attached to the nanomanipulator by depositing platinum to the contact surface (Figure 6, e). After that, the lamella's final side was detached from the specimen by milling (Figure 6, f), and the lamella was lifted out (Figure 6, g) by lowering the sample holder and moved further away (Figure 6, h). After locating the correct TEM grid, resetting the eucentric position and inserting the nozzle, the lamella could be moved closer to a grid while adjusting the movement direction (Figure 6, i) and transported into contact with a TEM grid. The lamella was attached to a grid using the Pt deposition (Figure 6, j) and was disconnected from the nanomanipulator by milling the connection between (Figure 6, k and m). Then final thinning at lower beam currents (Figure 7) and polishing processes at lower voltages were completed. In the case of lamellae, the area of interest for further TEM studies with higher magnification is the cross-section of the thin-film nanolaminate structure, located between the substrate and protective Pt layer (Figure 9, black arrows).

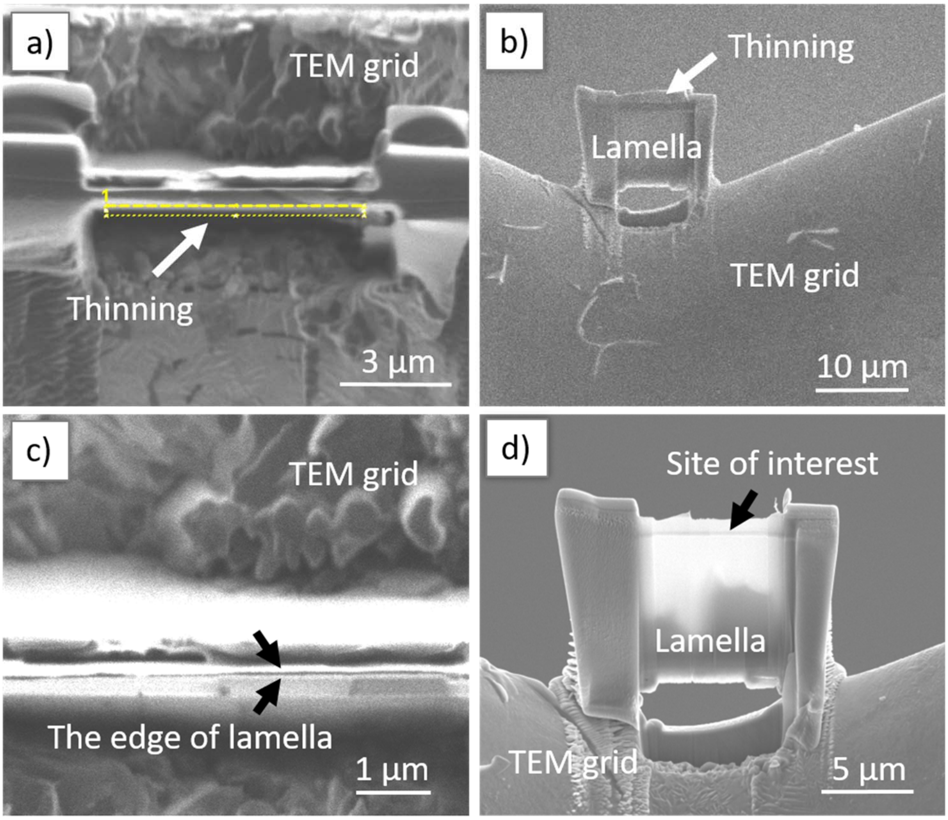

Figure 7. Focused ion beam (a, c) and electron beam (b, d) view of the thinning process of the lamella (a, b) and the result of the thinning (c, d). Black arrows indicate the edge of lamella (c) and site of interest (d) for TEM studies.

The lamella attached to the lift-out type TEM grid was carefully transported and inserted into a TEM specimen holder (Figure 8) for TEM studies. Scanning transmission electron microscopy (STEM) and high-resolution transmission electron microscopy (HRTEM) studies for the characterization of the cross-sections of the nanolaminate structures were carried out using FEI Titan Themis 200 instrument with a field emission gun operated at 200 kV [**III–V**]. The device was equipped with a probe C_s corrector and a Bruker SuperX silicon drift detector (SDD) energy-dispersive X-ray spectroscopy system. The EDX system was used for the composition profiling of the nanolaminates [**III, IV**].

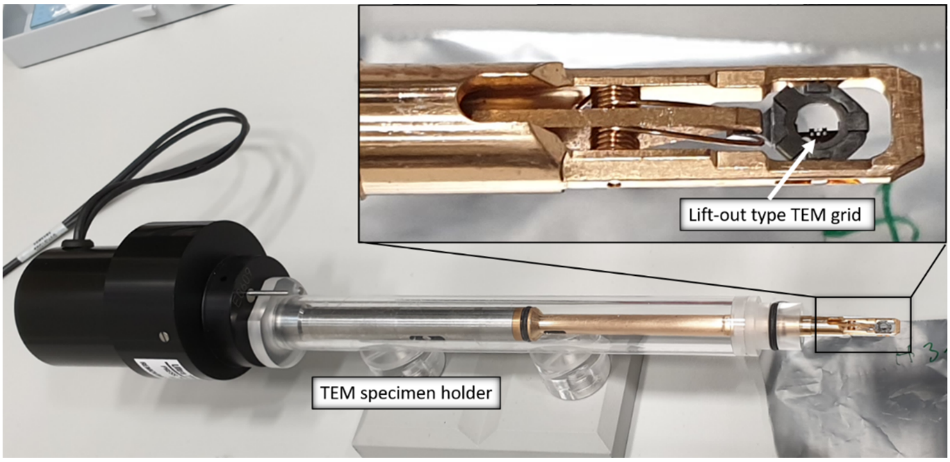

Figure 8. A photo of the TEM specimen holder. The arrow on the enlarged inset points to the lift-out type TEM grid to which a lamella made out of the sample has been previously attached in the SEM-FIB device. Lamella itself cannot be seen from this photo due to its small dimensions.

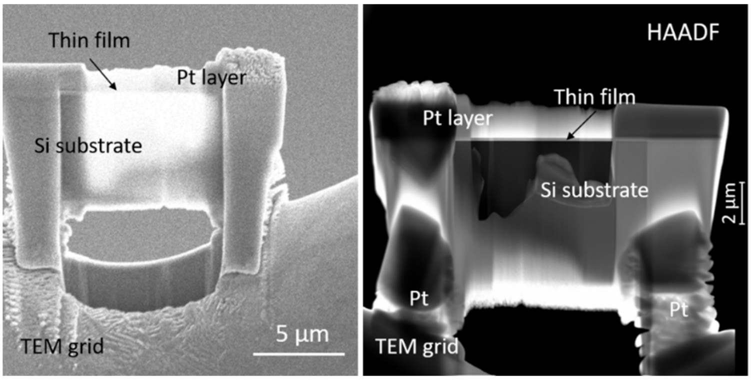

Figure 9. SEM image of one side of the lamella (left panel) after the thinning process has been completed and HAADF STEM image of the same lamella from the opposite side (right panel). The black arrow indicates the site of interest (deposited nanolaminate) between the Si substrate and protective Pt layer, which is later closely examined (with higher magnification).

Selected samples deposited on a silicon substrate were subjected to magnetic measurements [**I**–**V**]. These measurements were performed at room temperature [**I**–**V**] and 2 K [**IV**, **V**] using the P525 Vibrating Sample Magnetometer (VSM) option of the Physical Property Measurement System (PPMS) 14T (Quantum Design) located in Tallinn at the National Institute of Chemical Physics and Biophysics. Measurements at room temperature were preferred considering potential applications. Even if the experiments at low temperatures (i.e., those approaching that of liquid nitrogen or even absolute zero) would show higher magnetization and stronger coercive force compared to the experiments carried out at room temperature, it would be complicated and unreasonable to implement such an environment for the desired field of application. In practice, the devices designed for customary electronics must function at temperatures markedly higher than 300 K. Rectangular samples were fixed with GE-7031 varnish to the commercial quartz sample holders (Quantum Design) (Figure 10) before the experiment. This holder was, in turn, attached to the sample rod and inserted into the PPMS device. The magnetic hysteresis loop of the material was recorded by sweeping the external magnetic field applied parallel to the film surface and recording the material's response to the applied magnetic field in the form of magnetization.

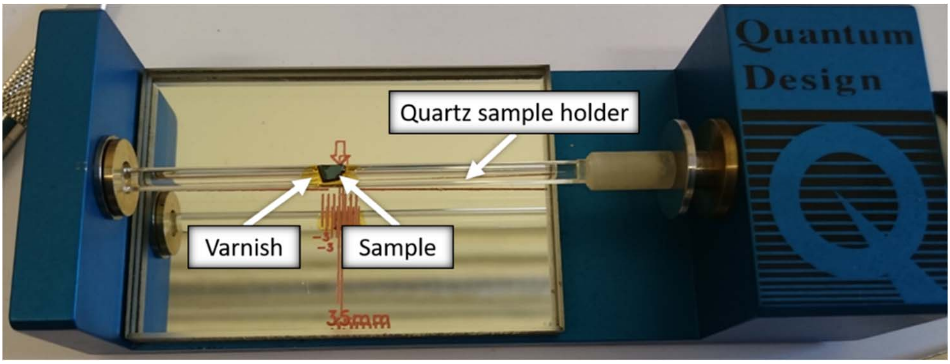

Figure 10. Sample fixed on a quartz sample holder with a varnish for VSM measurements. The orange scale on the Quantum Design sample-mounting station that can be seen below the quartz sample holder indicates a reference scale to position the sample optimally for detecting coils.

Some indications of ferromagnetic-like behaviour in such curves are a nonlinear response to the applied external magnetic field, presence of saturative magnetization and measurable coercivity. The saturation magnetization (M_S) describes a state where increasing the applied external magnetic field does not increase the magnetization value of the material further. Coercivity (H_C) is the value of the magnetic field at the moment when the magnetization of material has been reduced back to zero. The range in which the magnetic field strength was swept depended on the materials studied. In the case of some materials sweeping in a broader range was required to see the formation of saturation magnetization (for example, sweeping up to 40000 Oe). Structures deposited on undoped silicon substrates were preferred for magnetic measurements instead of doped or TiN layer containing substrates to avoid possible interferences by magnetization signal and noise from the substrates. In addition, the diamagnetic signal arising from the pure silicon substrate was subtracted from the general magnetization curve for all of the samples in which a ferromagnetic-like response was detected.

Before carrying out the electrical measurements, metal-insulator-metal (MIM) capacitor stacks were constructed based on samples deposited on a conductive substrate, which was highly doped conductive silicon covered by TiN layer as described above [**I**–**V**]. Pt [**III**] or Ti/Al double-layer [**I, II, IV, V**] dot electrodes with an area of 0.204 mm^2 were formed by electron beam evaporation through a shadow mask to the top of the ALD structure. The thicknesses for the Pt layer were 50 nm, 30–50 nm for Ti layers, and 110 or 120 nm for Al layers. Backside ohmic contact was provided by evaporating a 100–120 nm thick Al layer to the bottom side of the Si substrate.

Electrical measurements were carried out at the University of Valladolid in a light-proof and electrically shielded box using a Keithley 4200SCS semiconductor analyzer and Agilent DXO-X 3104 digital oscilloscope with a built-in wave generator. As parts of the electrical characterization, current-voltage (I-V) and charge polarization-voltage (P-V) measurements were carried out.

An I-V curve allows investigating the resistance characteristics of the device. During this measurement, the applied voltage is swept from positive to negative values (and vice versa), and the conduction current is measured. From these curves, it is possible to determine whether the material demonstrates an electric field-induced resistive switching effect, which is a sudden non-volatile and reversible change in resistance under the influence of a strong electric field. Typical systems that can take advantage of the resistive switching effect are, for example, capacitors [4, 78, 79], non-volatile resistive random-access memories [2–6, 78, 80–82] and memristor devices [4, 79, 82].

P-V measurements are carried out through the Sawyer-Tower circuit, which is used to characterize ferroelectric materials and study fundamental phenomena, such as spontaneous and remnant polarization, coercive-field and polarization reversal mechanisms [83]. In order to measure the polarization charge dependence on applied voltage characteristics, voltage is applied to the capacitive elements in the Sawyer-Tower circuit and swept and corresponding polarization charges are registered. If the material has ferroelectric properties, a hysteresis loop will be formed on this graph as a result of this measurement. The standard Sawyer-Tower experiment used in this study comprised applying a periodic triangular-shaped stimulus and recording the voltage loops data from the oscilloscope [**II**–**V**]. Charge values were obtained from the sensed voltage across a known capacitance [**II**–**V**].

RESULTS AND DISCUSSION

Structure and morphology

The phase composition strongly influences the properties of the deposited thin films and nanolaminates. The phase composition itself can depend on several factors, including different deposition parameters (growth recipe, deposition temperature, to name the most important). Stabilizing specific metastable phases in the material might enhance the material's behaviour due to the phase's specific nature, making it an attractive outcome from the current Thesis point of view. In addition, investigating the morphology and cross-sections of the nanolaminates can, for example, confirm that the intermediate layer has been completely formed, provide valuable information about thicknesses of the interlayers, uniformity and surface morphology of the deposited structures. For the complete analysis and (additional) information regarding growth rates, cycle ratios, cation ratios and thicknesses, not separately mentioned in this chapter, one can refer to original publications [**I**–**V**].

Studies on the grazing incidence X-ray diffraction (GIXRD) patterns of the Fe_2O_3-BiOCl composites and respective reference films [**I**] showed that all but one thin composite were crystallized in the as-deposited state. The phases present were orthorhombic ε-Fe_2O_3 and tetragonal BiOCl [**I**] (Table II); no $BiFeO_3$ could be detected. This orthorhombic ε-Fe_2O_3 phase that was stabilized in these composites is known as a rare, synthetic and metastable phase synthesized and found only in nanoscale samples [23, 25, 84–86] and attractive due to its multiferroic properties [23–25]. The peak intensities varied noticeably, and the sample with the ALD growth cycle sequence 175 × Fe_2O_3 + 280 × BiOCl stood out from the other Fe_2O_3-BiOCl composites as the crystallographically most ordered one [**I**]. Studying the morphology of the samples with SEM showed that on all Fe_2O_3-BiOCl composites except for one thin composite, the surface was covered with grain-like features characteristic of crystallized thin film (and ε-Fe_2O_3 phase) and nanoflakes characteristic of BiOCl [**I**]. Their appearance depended on the number of cycles applied to grow the constituent layers [**I**]. The average size of these grain-like features increased as the thickness of the Fe_2O_3 layer increased [**I**]. This led to the proposal that the BiOCl nanoflakes did not uniformly cover the Fe_2O_3 layer, which was also confirmed after investigating the cross-sections of the selected samples [**I**]. The Fe_2O_3 layer was uniform and its thicknesses matched with the thicknesses calculated from the XRF results [**I**]. For BiOCl, the width of randomly selected nanoflakes of the investigated sample ranged from 8 to 29 nm [**I**].

Annealing the reference samples and Fe_2O_3-BiOCl composites in the air environment at 800 °C for 30 min resulted in a phase change from an orthorhombic ε-Fe_2O_3 to rhombohedral α-Fe_2O_3 (hematite), and from tetragonal BiOCl to cubic and monoclinic Bi_2O_3 polymorphs [**I**]. Although the desired outcome would have been the formation of a bismuth ferrite containing interface, these phase changes were somewhat expected because annealing can reduce the amount of Cl in the composition. Furthermore, the metastable ε-Fe_2O_3 phase is thermally very unstable and has been observed as an intermediate phase between stable γ-Fe_2O_3 (maghemite) and α-Fe_2O_3 phases upon heating [23, 87, 88]. Annealing also noticeably changed the morphology of the samples as the nanoflakes had disappeared. The morphology of the three composites looked similar as they had areas covered with grain-like features neighbouring lighter plateau-like areas with distinctive boundaries between them [**I**]. The regions covered with grain-like features contained more Fe, and the concentration of these features increased together with the Fe_2O_3 layer thickness, thus indicating the contribution of Fe_2O_3 [**I**]. On the other hand, the plateau-like areas contained more bismuth compared to the darker grainy areas [**I**].

While studying the Er_2O_3-Fe_2O_3 mixed thin films, it could be seen that the film with very low Er content (that is, film grown using the Er_2O_3:Fe_2O_3 cycle ratio of 1:1 that resulted in Er/Fe cation ratio <0.002) revealed crystal growth and the presence of rhombohedral α-Fe_2O_3 (hematite) (Table II) [**II**]. The 4 nm thick reference Er_2O_3 film was not entirely amorphous and exhibited a nanocrystalline nature as one broadened reflection was present [**II**]. The films grown with cycle ratios that resulted in larger erbium-to iron cation ratios occurred essentially amorphous [**II**]. An exception was the film grown with the Er_2O_3:Fe_2O_3 cycle ratio of 50:5, where the partial formation of the nanocrystalline $ErFeO_3$ could be considered. However, due to the broad peak and low amount of peaks, the phase determination remained incomplete [**II**]. The surface morphology of the mixed thin films was relatively smooth and depended on the growth recipe to some extent [**II**]. While comparing the morphology of the mixed films deposited using the Er_2O_3:Fe_2O_3 cycle ratios of 1:1, 50:1, 50:5 and 300:20, it was noticed that high relative amounts of Er_2O_3 in growth cycles (for example, 300:20) resulted in amorphous and smoother films compared to those grown using lower relative amounts of Er_2O_3 in growth cycles (for example, 1:1) [**II**]. Tiny grain-like features were present on the bird-eye view SEM images of mixed films grown using the cycle ratios of 50:5 and 50:1, which could be small-sized agglomerations of disordered material present on the surface [**II**]. For detailed information regarding the growth cycle ratios and sequences, resulting Er/Fe atomic ratios and thicknesses, one can refer to the original publication [**II**].

The ZrO_2-Co_3O_4 nanolaminates and reference thin films [**III**] were crystallized in the as-deposited state. The phases present in the reference thin films were cubic and monoclinic ZrO_2 and cubic Co_3O_4 (Table II) [**III**]. In the 5-layer-nanolaminates, the cubic Co_3O_4 was still present, and the dominant phase was the cubic ZrO_2 polymorph (Table II) [**III**]. The presence of the tetragonal ZrO_2 phase could not be completely ruled out due to close locations of diffraction reflections. The peak intensities were noticeably higher for the nanolaminate that had the ZrO_2 as the topmost level, and therefore its interlayers are more ordered compared to the other nanolaminate [**III**]. SEM images of the ZrO_2-Co_3O_4 nanolaminates and reference thin films showed the grain-like features related to crystallization covering the surfaces of the samples uniformly [**III**]. The similarities between the samples with the same type of oxide as the topmost layer lead to the implication that the layers of the nanolaminates were not mixed [**III**]. In addition, the charging effect was noticed in the case of the ZrO_2 layers, recognized by the bright white areas visible on the SEM images [**III**], which is more characteristic of the non-conductive (insulating) materials. This can be important because, in Ramesh *et al.* [89], it has been stated that, in order to be ferroelectric, a material must be insulating as otherwise, the mobile charges would screen out the electric polarization [**III**]. STEM images and cross-sectional EDX composition profiling showed five distinct metal oxide layers grown sequentially on a substrate [**III**] (Figure 17). The oxygen signal was detected homogeneously across all metal oxide layers, and chemically distinct cobalt- and zirconium-containing oxide layers alternated as expected [**III**] (Figure 17). Slight mixing of layers had occurred at the interfaces between the oxide layers [**III**]. The thicknesses of the oxide layers were similar to each other, except the first layer of $2 \times (Co_3O_4 + ZrO_2) + Co_3O_4$ nanolaminate that occurred slightly thicker compared to other layers [**III**] (Figure 17).

The dominant phases present in the ZrO_2-Al_2O_3 mixed films/nanolaminates and in the 45 nm thick ZrO_2 reference thin film were metastable ZrO_2 phases, i.e. cubic or tetragonal polymorph (Table II) [**IV**]. Determining the exact ZrO_2 metastable phases (cubic, tetragonal, orthorhombic) present in the samples is complicated due to the close locations of these diffraction reflections corresponding to different phases and the nanocrystalline nature of the material resulting in broader reflections [**IV**]. In addition to metastable phases, the presence of stable monoclinic ZrO_2 phase was recognized in the ZrO_2 reference sample and two nanolaminates, including the nanolaminate with the thickest Al_2O_3 layers (Table II) [**IV**]. The bird-eye view SEM images of ZrO_2 reference thin film and ZrO_2-Al_2O_3 films showed that the surface was uniformly covered by grain-like features related to crystal growth [**IV**]. The surface of reference ZrO_2 thin film was quite rough, according to the size of the grains, and in the ZrO_2-Al_2O_3 films, the lateral grain size further decreased as the Al_2O_3 content increased [**IV**]. The HRTEM images of the cross-sections of ZrO_2-Al_2O_3 films revealed that the ZrO_2 layers were nanocrystalline and not perfectly smooth [**IV**]. The crystallization extended through neighbouring constituent layers, and the interfaces present in-between the oxides were relatively diffuse [**IV**]. This roughness is higher partly because the material has grown as mainly polycrystalline, and these irregularities increased as the number of constituent oxide growth cycles decreased. The thin Al_2O_3 layers between the ZrO_2 layers became very weakly distinguishable when smaller numbers of Al_2O_3 ALD cycles per layer (1 or 6) were used [**IV**]. Quite expectedly, the distinction between different layers became more evident in the case of the sample with slightly thicker Al_2O_3 and ZrO_2 constituent layers deposited using the 10 and 200 ALD cycles per layer, respectively [**IV**]. The crystallographic structure of the nanolaminates was resistant against annealing up to approximately 1000 °C. At temperatures reaching 1000–1200 °C, the metastable composition of nanolaminates and mixed films appeared to be sensitive to the annealing as the degree of crystallization increased. However, after cooling the films, the phase transition occurred and resulted in a marked contribution from the stable crystallographic phase.

Table II. An overview of the phase compositions of deposited structures in the as-deposited state. In most samples, in the case of the ZrO_2 and HfO_2, three metastable phases are all listed in the table due to the abovementioned complications in determining the exact metastable phases present in the samples.

Type of study	Type of sample	Identified phases
Fe_2O_3-BiOCl composites [**I**]	Fe_2O_3 reference	orthorhombic ε-Fe_2O_3
	BiOCl reference	tetragonal BiOCl
	Fe_2O_3-BiOCl composites	orthorhombic ε-Fe_2O_3, tetragonal BiOCl
Er_2O_3-Fe_2O_3 mixed films [**II**]	Er_2O_3 reference	nanocrystalline cubic Er_2O_3
	Mixed film with Er_2O_3:Fe_2O_3 cycle ratio of 1:1 (Er/Fe cation ratio <0.002)	rhombohedral α-Fe_2O_3 (hematite)
	Mixed films with Er_2O_3:Fe_2O_3 cycle ratios of 3:1, 60:3, 50:1, 300:20 (resulting in the Er/Fe cation ratios of 0.02, 0.46, 0.26, 0.18, respectively)	(amorphous)
	Mixed film with the Er_2O_3:Fe_2O_3 cycle ratio of 50:5 (Er/Fe cation ratio 0.30)	partially orthorhombic $ErFeO_3$
ZrO_2-Co_3O_4 nanolaminates [**III**]	ZrO_2 reference	cubic ZrO_2, monoclinic ZrO_2
	Co_3O_4 reference	cubic Co_3O_4
	Co_3O_4-ZrO_2 nanolaminates	cubic and/or tetragonal ZrO_2, cubic Co_3O_4
ZrO_2-Al_2O_3 mixed films and nano-laminates [**IV**]	ZrO_2 reference	monoclinic ZrO_2, cubic, tetragonal and/or orthorhombic ZrO_2
	Nanolaminates with ZrO_2:Al_2O_3 cycle ratio of 120:6 and 200:10	monoclinic ZrO_2, cubic, tetragonal and/or orthorhombic ZrO_2
	Mixed film with ZrO_2:Al_2O_3 cycle ratio of 100:1	cubic, tetragonal and/or orthorhombic ZrO_2
HfO_2-Al_2O_3 mixed films or nanolaminates [**V**]	HfO_2 reference	monoclinic HfO_2, orthorhombic, cubic, and/or tetragonal HfO_2
	Nanolaminates with HfO_2-Al_2O_3 cycle ratios of 300:5, 200:10 (15 nm and 10 nm as nominal HfO_2 layer thicknesses and ca. 0.25–0.5 nm as Al_2O_3 layer thicknesses) Mixed film with 100:1 cycle ratio	orthorhombic, cubic, and/or tetragonal HfO_2, monoclinic HfO_2
	Nanolaminates with HfO_2-Al_2O_3 cycle ratios of 170:10, 120:6, 100:5 (nominal HfO_2 and Al_2O_3 layer thicknesses in the range of ca. 5–8 nm and ca. 0.25–0.5 nm, respectively)	orthorhombic, cubic, and/or tetragonal HfO_2, monoclinic HfO_2, (partly amorphous)

In a study on HfO_2-Al_2O_3, the ALD cycle ratio was varied between 200:10 and 15:1 to grow nanolaminates and mixed films and study the stabilization of the metastable HfO_2 polymorphs. The HfO_2 metastable phases to consider are orthorhombic, cubic and tetragonal polymorphs [**V**]. The 42 nm thick HfO_2 reference film consisted of stable monoclinic phase and metastable phases (Table II) [**V**]. HfO_2-Al_2O_3 samples could be regarded as multiphase materials with contribution from both metastable and stable HfO_2 polymorphs (Table II) [**V**]. Compared to the reference thin film, the contribution from the metastable polymorphs had strengthened [**V**]. This demonstrates the importance of using the approach of combining HfO_2 with amorphous Al_2O_3 to stabilize metastable phases. The amorphous background appeared on the GIXRD patterns of some nanolaminates with nominal HfO_2 and Al_2O_3 layer thicknesses in the range of ca. 5–8 nm and ca. 0.25–0.5 nm, respectively. In some of these samples, the extent of the amorphous background made the presence of a stable monoclinic phase harder to confirm (Table II) [**V**]. Annealing these lower nominal layer thickness samples reduced the amorphous background, increased the crystallinity of the films, and the contribution from monoclinic polymorph became apparent [**V**].

Therefore, the metastable phases were successfully stabilized and even dominated the phase composition in several multilayer structures. The strengthened contribution from metastable polymorphs in the case of multilayer structures was observed in ZrO_2-Al_2O_3 [**IV**] and HfO_2-Al_2O_3 [**V**] samples. The metastable ε-Fe_2O_3 could also be stabilized in the as-deposited state, and annealing resulted in a phase change to a stable α-Fe_2O_3 phase [**I**]. Morphology studies revealed that, in general, the surface morphology depended on the growth recipe and resulting thicknesses to some extent. In the case of ε-Fe_2O_3, Co_3O_4, ZrO_2 and HfO_2, grain-like features related to crystal growth covered the surfaces uniformly. However, the BiOCl nanoflakes in Fe_2O_3-BiOCl composites did not uniformly cover the uniform Fe_2O_3 layer, which might negatively influence the electrical properties of these samples [**I**]. Due to the polycrystalline nature, the ZrO_2 layers in the ZrO_2-Al_2O_3 films cross-sectional studies appeared rather rough, and the irregularities increased as the number of constituent oxide growth cycles decreased [**IV**]. Quite expectedly, the distinction between different layers became more evident in the sample with slightly thicker Al_2O_3 and ZrO_2 constituent layers.

Conformality of the thin film growth to 3D substrates

As mentioned above, ALD is known for its ability to uniformly cover high aspect ratio 3D structures and complicated deep cavities [31, 32, 40, 44]. Achieving high uniformity usually requires parameters optimization, such as changing cycle time parameters (pulse and purge lengths) or temperature or pressure. In the current study, optimizing the parameters separately for 3D substrates was not performed, as the growth experiments were conducted on all substrates simultaneously. That way, it was possible to examine whether the reasonably short ALD cycle lengths and film thicknesses providing sufficient magnetic properties and conformal growth to 3D substrates could be partially combined. The deposited thin film's ability to follow the shape of the 3D substrate was studied for the ε-Fe_2O_3 reference and two-layer sample 175 × Fe_2O_3 + 280 × BiOCl deposited to trenches with the 60:1 aspect ratio [**I**], and Er_2O_3:Fe_2O_3 film with cycle ratio 3:1 deposited to stacks with the 20:1 aspect ratio [**II**].

Investigating the bird-eye view (Figure 11) and cross-section (Figure 12, [**I**]) SEM images of the ε-Fe_2O_3 reference sample and Fe_2O_3-BiOCl sample confirmed that the film had followed the shape of the 3D substrate during the deposition as it should be characteristic to ALD. The regular pattern of the holes present on the bird-eye view SEM image of the ε-Fe_2O_3 reference sample (Figure 11, left panel) indicated that the closing of the trenches' openings was avoided [**I**]. The Fe_2O_3 thin film was grown almost uniformly to the inner regions of the 3D substrate, reaching the bottom of the ~ 6 µm deep 3D substrate [**I**]. However, the thickness of the layer decreased noticeably towards the bottom of the trench, which means that the step coverage was not 100 % for these deposition parameters [**I**]. There were fewer openings to the trenches visible on the bird-eye view SEM image of the Fe_2O_3-BiOCl sample (Figure 11, right panel), probably due to BiOCl nanoflakes closing and covering the openings (Figure 12). These BiOCl flakes were mainly formed on the easily accessible upper part of the trench (Figure 12), as expected, although some flakes were formed deeper inside the trenches [**I**].

According to the cross-section of the Er_2O_3:Fe_2O_3 film with cycle ratio 3:1, the thin film had successfully reached the bottom of the stack, although the nucleation of the thin film layer was not uniform throughout the whole depth [**II**].

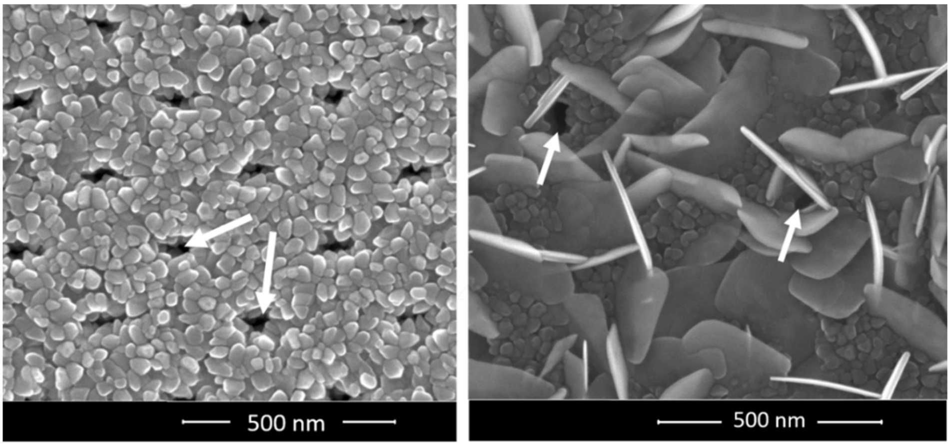

Figure 11. The bird-eye view SEM images of the Fe_2O_3 reference thin film (left panel) and two-layer Fe_2O_3-BiOCl sample grown using the cycle sequence of 175 × Fe_2O_3 + 280 × BiOCl (right panel) on the 3D substrate. The tips of the white arrows point to some of the openings of the trenches [**I**].

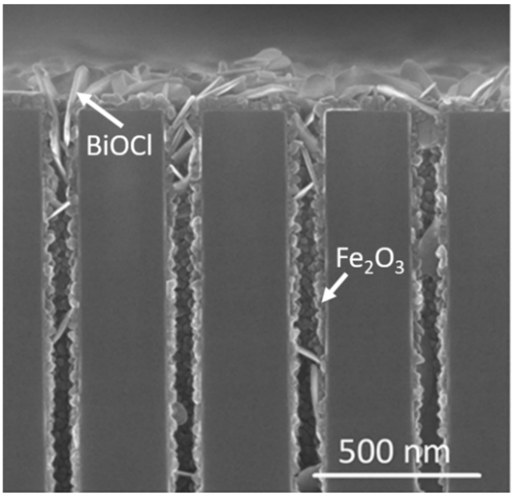

Figure 12. Cross-section view SEM image of the upper part of the two-layer Fe_2O_3-BiOCl sample grown using the cycle sequence of 175 × Fe_2O_3 + 280 × BiOCl on 3D substrate [**I**].

These studies on films deposited to 3D trenched structures demonstrated that the ε-Fe_2O_3 thin film and Er_2O_3:Fe_2O_3 mixed film could be successfully grown to the inner regions of challenging 3D substrates, even though the step coverage of 100 % was not achieved with the current deposition parameters. This possibility to deposit thin films to the inner regions of 3D substrates is considered a prerequisite for possible applications in the memory devices and semiconductor industry.

Magnetic properties

Nanostructured materials can often demonstrate unique magnetic characteristics [90–93]. Magnetic properties of thin-film nanostructures can, besides chemical composition, significantly depend on several other factors such as defects (for example, vacancies) [94–99], phase [23, 44, 99], thickness [44, 100] and growth recipe [**II,** 99, 100]. Quite commonly, it can be a combination of several factors contributing to the material's magnetic properties, therefore, making it less unambiguous to interpret the results and more challenging to detect which influencing factor is responsible for such a response. For example, in the context of the current study, ferromagnetic-like response.

In the present study, the magnetic measurements were performed to Fe_2O_3-BiOCl composites [**I**], ZrO_2-Co_3O_4 nanolaminates [**III**] and corresponding reference thin films [**I**, **III**], Er_2O_3-Fe_2O_3 mixed thin films [**II**], ZrO_2-Al_2O_3 nanolaminates [**IV**], and HfO_2-Al_2O_3 nanolaminates [**V**]. Most of the recorded magnetic hysteresis loops showed nonlinear and saturative magnetization and measurable coercivity [**I**–**V**]. Thus, most of the samples subjected to magnetic measurements demonstrated ferromagnetic-like behaviour at room temperature [**I**–**V**], but the main and distinguishable factors contributing to the apparent hysteretic behaviour varied in terms of material layers composition, phase, and thickness.

Out of all the investigated samples, the highest coercivity value recorded was 9757 Oe (776.4 kA/m), which was measured for both the Fe_2O_3 reference and one Fe_2O_3-BiOCl composite (Figure 13, Table III), having the ε-Fe_2O_3 phase being the main contributor to the higher coercivity value [**I**]. The same Fe_2O_3-BiOCl sample was also crystallographically more ordered compared to the other Fe_2O_3-BiOCl composites as its diffractogram showed higher ε-Fe_2O_3 phase-related peak intensities [**I**], therefore, indicating that the crystallographic ordering can also influence magnetization. The magnetic properties of Fe_2O_3-BiOCl composites were further investigated after annealing the composites at 800 °C for 30 minutes. In general, annealing these composites resulted in noticeably reduced magnetic behaviour [**I**], and the coercivity value remained several times lower compared to the as-deposited measurements [**I**]. For example, the coercivity value of sample 80 × Fe_2O_3 + 280 × BiOCl decreased from 4230 Oe (337.4 kA/m) to 35 Oe (2.79 kA/m) after annealing [**I**] (Figure 13). The saturation magnetization in this 80 × Fe_2O_3 + 280 × BiOCl sample increased from 29 emu/cm^3 to 175 emu/cm^3 [**I**] (Figure 13). For the rest of the Fe_2O_3-BiOCl composites, the saturation magnetization decreased after annealing [**I**] (Figure 13). This time the main reason for the change in magnetic behaviour was plausibly the Fe_2O_3 phase change from orthorhombic ε-Fe_2O_3 to rhombohedral α-Fe_2O_3 [**I**].

Investigating the magnetic properties of Er_2O_3-Fe_2O_3 mixed thin films [**II**] drew attention to the connection between the properties and the ALD growth recipe. It could be noticed that regardless of the smaller thickness (5.7 nm), the film deposited using relatively large amounts of growth cycles separately for constituent oxides demonstrated a markedly stronger magnetization compared to the more homogeneously mixed Er–Fe–O films [**II**]. Its saturation magnetization value was 5.3 emu/m^2 [**II**]. The correlation between the Er/Fe cation ratio and the magnetization was not recognized [**II**].

Investigating the magnetic properties of two five-layer ZrO_2-Co_3O_4 nanolaminates [**III**] and corresponding reference thin films revealed that both reference samples and one nanolaminate exhibited a similar response to the external magnetic field [**III**]. The coercivity value of the reference thin films was 60 Oe (Table III). Coercivity values of the nanolaminates were close to each other – 21 Oe and 32 Oe, respectively for 2 × (ZrO_2 + Co_3O_4) + ZrO_2 and 2 × (Co_3O_4 + ZrO_2) + Co_3O_4 (Table III). But a nanolaminate that had one ZrO_2 layer more and one Co_3O_4 layer less compared to the other nanolaminate showed several times higher saturation magnetization value, which was 1.7×10^{-5} emu [**III**] – indicating the potential contribution from nanocrystalline cubic-tetragonal ZrO_2 phases to such magnetization. This connection was in accordance with earlier studies on ZrO_2 films and nanoparticles, where magnetic behaviour had been reported and attributed mainly to the presence of oxygen-deficient metastable zirconia phases [**III**, 101–103], especially to the tetragonal ZrO_2 phase due to the presence of oxygen vacancies [**IV**, 104]. Furthermore, a similar contribution from metastable ZrO_2 phases to magnetization was seen for the ZrO_2-Al_2O_3 [**IV**] nanolaminates.

Simultaneously, no clear correlation between magnetization and content of aluminium in the ZrO_2 host material could be seen [**IV**].

Similarly to the ZrO_2, the magnetization in HfO_2 films has been previously explained by the presence of oxygen [95–98] or Hf [105] vacancies. In our study on HfO_2-Al_2O_3 nanolaminate films [**V**], both stable and metastable HfO_2 phases were present. Still, dominant metastable phases and related vacancies could be seen as one of the contributors to magnetization [**V**].

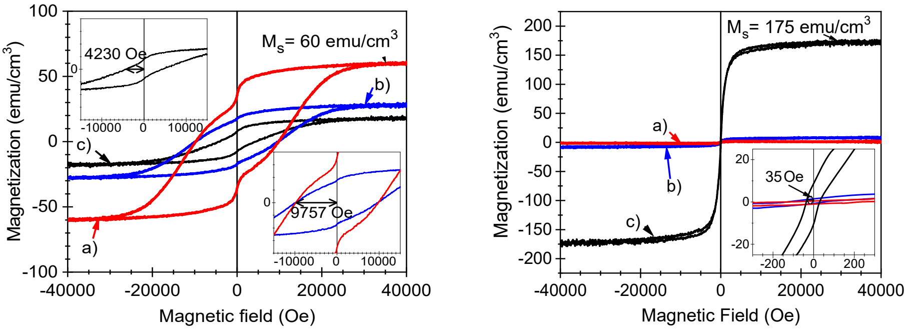

Figure 13. Magnetization vs external magnetic field (M-H) curves of the three samples that exhibited the highest coercivity values in the as-deposited state – a) 250 × Fe_2O_3, b) 175 × Fe_2O_3 + 280 × BiOCl, and c) 80 × Fe_2O_3 + 280 × BiOCl (left graph), and the M-H curves of the same samples after annealing (right graph). These curves were measured at 300 K, and substrate diamagnetism was subtracted from the data. The values on the inset figures indicate the coercivity (H_C) values. M_s shows saturation magnetization values.

Table III. An overview of the measured coercivity values of the selected samples. Coercivity values are measured at room temperature. The respective ALD structure description and total thickness are added to the table as a reference.

Type of study	ALD structure description	Total thickness (nm)	Coercivity (Oe)
Fe_2O_3-BiOCl [**I**]	250 × Fe_2O_3	46	9757
	175 × Fe_2O_3 + 280 × BiOCl	50	9757
	80 × Fe_2O_3 + 280 × BiOCl	33	4230
Er_2O_3-Fe_2O_3 [**II**]	2 × (300 × Er_2O_3 + 20 × Fe_2O_3) + 300 × Er_2O_3	5.7	5
ZrO_2-Co_3O_4 [**III**]	250 × ZrO_2	32	60
	250 × Co_3O_4	15	60
	2 × (200 × Co_3O_4 + 100 × ZrO_2) + 200 × Co_3O_4	64	32
	2 × (100 × ZrO_2 + 200 × Co_3O_4) + 100 × ZrO_2	60	21
ZrO_2-Al_2O_3 [**IV**]	5 × (120 × ZrO_2 + 6 ×Al_2O_3) + 120 × ZrO_2	38	85
HfO_2-Al_2O_3 [**V**]	3 × (200 × HfO_2 + 10 × Al_2O_3) + 200 × HfO_2	48	127

Even though magnetic measurements at room temperature were preferred considering potential applications, the measurements were in addition to room temperature also performed at 2 K for the ZrO_2-Al_2O_3 [**IV**] and HfO_2-Al_2O_3 [**V**] nanolaminate films. As a result, it was noticed that the coercivity was somewhat higher at low measurement temperatures, reaching the values of 200 Oe [**IV**] or 400 Oe [**V**] at 2 K, compared to 85 Oe [**IV,** Table III] or 127 Oe [**V,** Table III], recorded at room temperature. At the same time, there were no significant differences in the saturation magnetizations at different temperatures, as the maximum values at both temperatures stayed around 2×10^{-4} emu/g [**IV, V**].

Taken together, most of the samples subjected to magnetic measurements demonstrated ferromagnetic-like behaviour at room temperature. The ε-Fe_2O_3 containing specimens stood out from others in terms of several times higher coercivity (Table III) [**I**], reaching up to ~10 kOe. Metastable phases and related defects induced considerable magnetization in materials not as commonly known for their magnetic properties – ZrO_2 and HfO_2. It was also noticed that the magnetization was somewhat better realized in the laminates or layered structures than in mixed films. Furthermore, the appearance of magnetization in the multilayer structures and nanolaminates supports the goal of depositing materials with multiferroic properties by combining magnetically and electrically polarizing thin films into one nanolaminate.

Electrical behaviour

Electrical polarization

Electrical charge polarization – voltage (P-V) curves recorded during the Sawyer-Tower measurements provide information about the material's ferroelectric properties, the presence of which is one of the preconditions for a multiferroic material. Ferroelectric materials exhibit spontaneous polarization, which can be reversed by an applied electric field, resulting in nonlinear hysteresis loop formation (Figure 14) [106–108]. In the case of ferroelectric material, during hysteresis loop formation, charge in a material can be drawn to saturation in both polarity directions (Figure 14) [**V**, 109] – increasing the externally applied voltage does not further increase the charge value. When the voltage is swept back to zero, a remnant polarization charge can be recorded at zero bias voltage (Figure 14) [**V**, 106]. When the charge in the material is reduced back to zero under the influence of oppositely polarized voltage, the electrical coercivity can be measured (Figure 14) [106].

Similarly to magnetic materials, ferroelectric thin films and nanostructured materials can exhibit unique phenomena that are significantly distinguished from larger-sized ferroelectric systems [26, 27, 106]. One example is a different polarization behaviour, especially the coercive field, which is higher in thin films than in bulk materials [26, 106, 110, 111].

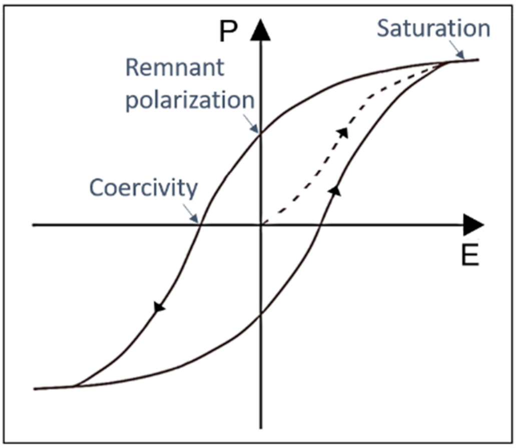

Figure 14. Illustrative polarization hysteresis loop typical of a ferroelectric material.

The results of the measured electrical charge polarization-voltage curves were discussed for the selected samples in studies **II–V**. The loops recorded of ZrO_2-Co_3O_4 nanolaminates based MIM capacitor stacks [**III**] did not exhibit saturation. The closed-loop had formed, but its shape was typical of a lossy dielectric [**III**, 106, 109] instead of a ferroelectric material.

The ZrO_2-Al_2O_3 nanolaminates based stacks [**IV**] behaved quite similarly compared to stacks in study **III** – the recorded loops were wider and more concave by shape, but no presence of saturation could be detected. The charge determined by electrical hysteresis measurements can be influenced by polarization, space charge (for example, oxygen vacancies) and leakage currents in thin films [106]. The charge polarizing in these ZrO_2-Al_2O_3 nanolaminates based stacks [**IV**] is likely caused by the carrier transport between Ti and TiN electrodes and interfacial polarization [**IV**]. The charge can become trapped at interface barriers between the ZrO_2-Al_2O_3 layers and at the interface between the ZrO_2 and TiN electrode, enhancing interfacial polarization and causing hysteretic behaviour [**IV**]. The charge polarization was higher in the nanolaminates compared to the ZrO_2 reference film, demonstrating the influence of internal interfaces between the ZrO_2-Al_2O_3 layers on charge polarization [**IV**].

The hysteresis loops of Er_2O_3-Fe_2O_3 based stacks [**II**] demonstrated charge polarization and were quite quadratic by shape, but the saturation plateau, usually characteristic of ferroelectric materials, was not detected. Even though somewhat similar behaviour in $ErFeO_3$ films has been previously interpreted as ferroelectric [112], in the current study, the polarization is likely again caused by the carrier transport between electrodes and interfacial polarization [**II**]. The charge is drifting and becomes trapped at the interfaces between metal oxide layers and electrode layers. When the opposite strong enough field is applied, the charges are released from the traps, causing charge polarization [**II**].

The features characteristic of ferroelectric materials could be better recognized on the hysteresis loops of HfO_2-Al_2O_3 based MIM capacitor stacks [**V**], including saturation as the charge could be drawn to saturation in both polarity directions (Figure 15, left panel) [**V**]. Therefore, the ferroelectric polarization component is likely present, but the loops were also affected by previously mentioned interfacial polarization due to considerable leakage currents [**V**]. It was noticed that the leakage effect influencing the polarization loop was somewhat stronger when HfO_2 content in the films increased [**V**]. The higher leakage effect can also be connected with the multiphase nature of these nanolaminates, i.e., the apparent presence of the monoclinic phase of HfO_2 in addition to orthorhombic, cubic, and/or tetragonal polymorphs, which makes the phase composition heterogeneous [**V**]. On the other hand, one of the contributors to the material's ferroelectric-like response is likely the stabilization of the orthorhombic HfO_2 phase, which is a metastable phase previously acknowledged for its ferroelectric properties [26–30]. Therefore, it is necessary to select process conditions that can stabilize this metastable phase and enable the corresponding ferroelectric response [27, 29]. One of the many influencing factors to consider is the HfO_2 thin film (layer) thickness and the related surface energy effects [26–30]. It has been reported that decreasing the thin film thickness can stabilize the orthorhombic phase [27, 29, 30].

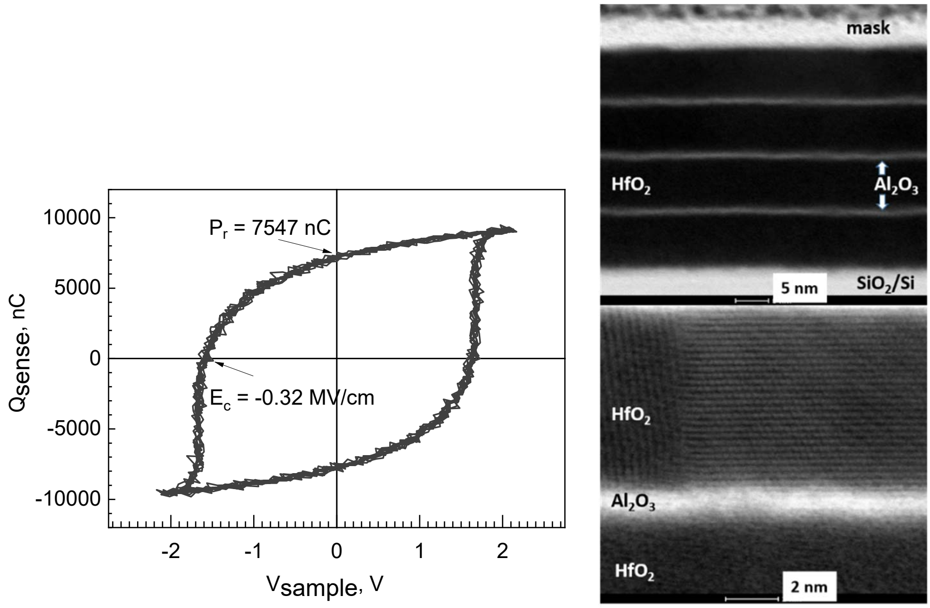

Figure 15. Electrical charge polarization – voltage (P-V) curve measured of HfO_2-Al_2O_3 nanolaminate based stack (left panel) [**V**]. P_r stands for remnant polarization, and E_c indicates coercivity. HRTEM cross-section images of the lamella made of the same type of nanolaminate grown using the HfO_2:Al_2O_3 cycle ratio of 200:10 (right panels). The upper image depicts the whole nanolaminate. The bottom panel shows the upper area of the nanolaminate [**V**].

When the thickness is increased, the phase gradually destabilizes in favour of the monoclinic phase [27], making it complicated to achieve an orthorhombic phase and corresponding ferroelectric-like response in thicker layers. In the current study, the formation of the HfO_2 orthorhombic phase was possible due to the amorphous Al_2O_3 layers (visible as light layers in HRTEM cross-section images on Figure 15, right panels), which were detected as thick enough to act as barrier layers to keep the HfO_2 layers separated. From these cross-section images, it could also be noticed that the crystal growth was more prominent in the upmost HfO_2 layer compared to the bottom layer(s) [**V**].

Therefore, in general, the charge polarization in investigated samples was noticeably dominated or affected by interfacial polarization caused by leakage currents that enabled charge accumulation at oxide/electrode interfaces [**IV**]. Only the HfO_2-Al_2O_3 nanolaminate based stacks showed an apparent saturation of the charge values together with defined remnant polarization and coercivity characteristic to a ferroelectric material, indicating the contribution from ferroelectricity along with the leakage currents. The stabilization of the ferroelectric phase was possible thanks to the alternation of fully formed Al_2O_3 and HfO_2 layers, the formation of which could be confirmed by investigating the HRTEM cross-section images.

Resistive switching

The recorded current-voltage (I–V) curve allows investigating the material's resistance characteristics, especially whether it demonstrates a current-induced resistive switching effect desired for resistive random-access memories [2–6, 78, 80–82]. This resistive switching effect is a sudden non-volatile and reversible change in the material's resistance under the influence of an applied voltage. Consequently, on the I–V graph of the material, two different resistance states can be distinguished – a high resistance state (HRS) and a low resistance state (LRS) (Figure 16). The resistive switching event from the HRS to the LRS (sudden decrease of resistance and a corresponding increase of the current) is called the SET process (Figure 16, left loops) [4, 5, 79]. The resistive switching event from LRS back to HRS (a sudden rise in resistance and a corresponding decrease of the current) is a RESET process (Figure 16, right loops) [4, 5, 79]. The voltages where the switching event occurs are V_{set} and V_{reset} for the SET and RESET processes, respectively [4].

The I–V curves for investigating the resistive switching characteristics of the deposited structures were studied in papers **I**, **III**, **IV** and **V**. The I–V loops recorded of ZrO_2-Co_3O_4 nanolaminates based MIM capacitor stacks demonstrated bipolar resistive switching behaviour (i.e., directional resistance switching depending on the polarity of the applied voltage [3]) in both samples but with opposite sign [**III**] (Figure 16). The different ordering of nanolaminates can be the reason for the opposite sign [**III**]. In the $2 \times (Co_3O_4 + ZrO_2) + Co_3O_4$ nanolaminate based stack (Figure 16), the switch from LRS to HRS occurred between –1.5 and –2.5 V and from HRS to LRS between 2.0 and 3.5 V, and both transitions were sharp [**III**]. In the $2 \times (ZrO_2 + Co_3O_4) + ZrO_2$ nanolaminate based stack, the SET occurred at about 6 V and RESET occurred between –6 and –8 V [**III**]. Both transitions were gradual, and loops were noticeably narrower [**III**]. According to the publication by A. Sawa [3], there are two main types of conducting bath: filamentary conducting path and an interface-type path. In the first case, the resistive switching originates from the formation (SET) and rupture (RESET) of conductive filaments in an insulating matrix, and it can be associated with both unipolar and bipolar switching behaviour [3]. In the second case, resistive switching occurs at the interface between the metal electrode and the oxide, and it is usually related to bipolar switching behaviour [3]. In the 2 × (Co_3O_4 + ZrO_2) + Co_3O_4 nanolaminate based stack, the presence of resistive switching effect is probably connected with the electrochemical migration of oxygen vacancies [**III**]. The electrochemical migration of oxygen vacancies close to the interface has been proposed to drive the resistive switching effect [3]. Besides, the density of oxygen vacancies also influences resistive switching [3]. In the 2 × (ZrO_2 + Co_3O_4) + ZrO_2 nanolaminate based stack, the dominant mechanism responsible for somewhat different resistive switching behaviour might be the migration of Co cations to the ZrO_2 layer (i. e., the electrochemical metallization of the layer) [**III**]. While comparing these nanolaminates in search for differences, one can notice, that the total thickness of the 2 × (Co_3O_4 + ZrO_2) + Co_3O_4 nanolaminate was only 4 nm thicker (64 nm) compared to the other nanolaminate. The impurities concentrations were relatively low for both nanolaminates, only slightly higher for 2 × (Co_3O_4 + ZrO_2) + Co_3O_4 nanolaminate [**III**]. On the other hand, the GIXRD diffractograms showed noticeably lower intensity peaks related to the ZrO_2 phases, indicating that the ZrO_2 phases in this nanolaminate can be crystallographically less ordered. The composition profiling confirmed that five layers were distinguishable (Figure 17) for both nanolaminates [**III**]. According to these similarities, it can be assumed that the reason for the different resistive switching behaviour is mainly the different ordering of nanolaminates.

The I–V curves of Fe_2O_3-BiOCl based stacks showed that the samples were moderately leaky, showed a rectifier-like behaviour and the conduction currents were affected by visible illumination as the current increased under illumination [**I**]. At the reverse bias, the device acted as a photovoltaic cell [**I**], which might be related to moderate band-gaps of the constituent compounds. The uneven surface of the composites could be the cause of leaky samples [**I**].

The I–V behaviour of ZrO_2-Al_2O_3 based MIM capacitor stacks was characteristic of resistive switching memory materials [**IV**]. The loops were highly repetitive, and the memory window between high and low resistance states was reproducible [**IV**]. Comparing the three films with different relative contents of Al_2O_3 with each other revealed that the higher the measured Al:Zr cation ratio, the narrower the voltage range in which the loops appear, and the wider the window between the high and low resistance states [**IV**]. Out of all the measured samples (including the ZrO_2 sample), the switching effect was most prominent in the ZrO_2-Al_2O_3 film with the highest Al:Zr cation ratio (0.30) [**IV**]. Even though the studied samples showed insulating behaviour, the resistive switching effect was enabled due to the samples' defective structure.

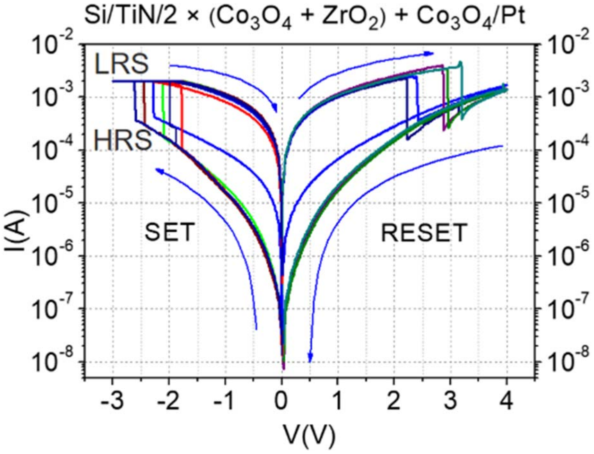

Figure 16. Current-voltage loops recorded of the 2 × (Co_3O_4 + ZrO_2) + Co_3O_4 nanolaminate based MIM capacitor stack [**III**]. The LRS marks the low resistance state, and HRS is the high resistance state.

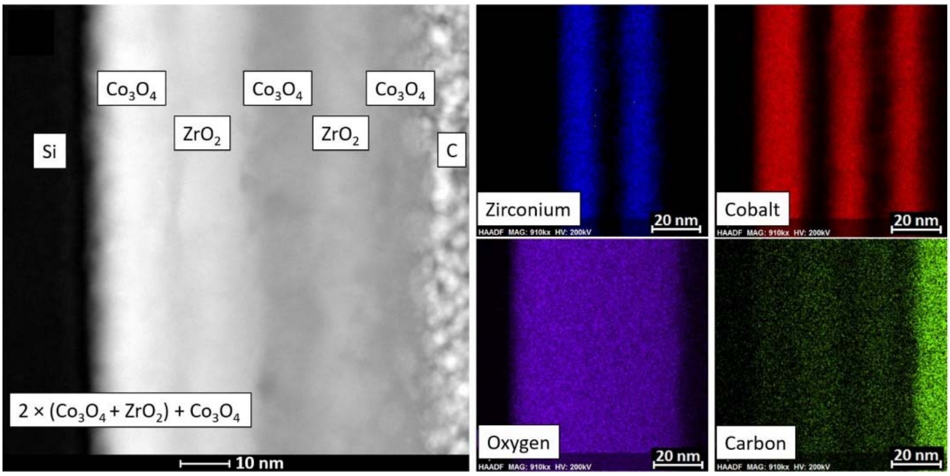

Figure 17. STEM image of the site of interest used during the composition profiling (left panel) and cross-sectional EDX composition profiling of the 2 × (Co_3O_4 + ZrO_2) + Co_3O_4 nanolaminate (right panel).

At the I–V curves of HfO_2-Al_2O_3 based MIM capacitor stacks, two distinctive resistance states at both positive and negative bias voltages characteristic of resistive switching memory materials were achieved [**V**]. The I–V curve of the HfO_2-Al_2O_3 nanolaminate based stack grown using the HfO_2:Al_2O_3 cycle ratio of 200:10 is displayed in Figure 18 for reference. The window between the high and low resistance state ranged over almost an order of magnitude [**V**].

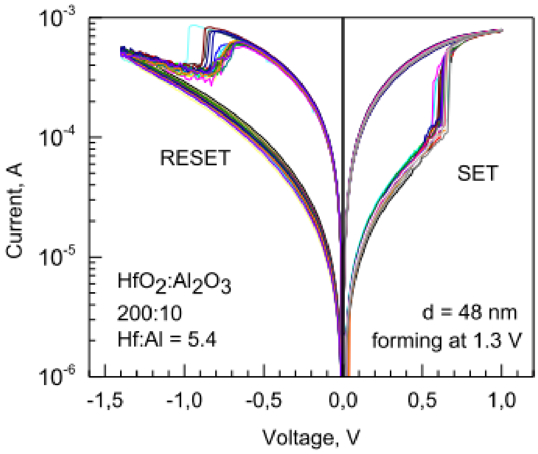

Figure 18. Current-voltage curve measured of the HfO_2-Al_2O_3 nanolaminate based stack grown using the HfO_2: Al_2O_3 cycle ratio of 200:10 [**V**]. The nanolaminate film thickness, d, is 48 nm, and 1.3 V indicates the electroforming voltage.

To conclude, the resistive switching effect was not observed in the Fe_2O_3-BiOCl based stacks [**I**]. These Fe_2O_3-BiOCl based stacks were moderately leaky and showed rectifier-like behaviour instead. On the other hand, ZrO_2-Co_3O_4 [**III**], ZrO_2-Al_2O_3 [**IV**] and HfO_2-Al_2O_3 [**V**] nanolaminates based stacks all demonstrated the resistive switching behaviour. The properties and extent of the resistive switching loops with their characteristic difference between high and low resistance states were affected by the composition and the order of the layers.

SUMMARY AND CONCLUSIONS

The purpose of this study was to contribute to the search and characterization of new and novel material combinations that would show ferromagnetic, ferroelectric and resistive switching behaviour at room temperature. The aim was to combine potentially ferromagnetic and ferroelectric materials (mainly metal oxides) into multilayer structures (nanolaminates) and mixed films. In the present Thesis, the atomic layer deposited multilayer structures studied were ZrO_2-Co_3O_4 nanolaminates, Fe_2O_3-BiOCl composites, Er_2O_3-Fe_2O_3 mixed thin-film structures, and ZrO_2-Al_2O_3 and HfO_2-Al_2O_3 mixed films and nanolaminates. The atomic layer deposition method was selected due to its ability to provide high-quality thin films and precise thickness control over large substrate areas through alternate self-limiting surface reactions. It has also already proven itself a suitable and widely used method in many research and industrial applications, including microelectronics.

The results showed that the metastable phases were successfully stabilized and even dominated the phase composition in several multilayer structures. The strengthened contribution from metastable polymorphs in the case of multilayer structures was observed in ZrO_2-Al_2O_3 and HfO_2-Al_2O_3 samples. The metastable ε-Fe_2O_3 could also be stabilized in the as-deposited state, and annealing resulted in a phase change to a stable α-Fe_2O_3 phase. Morphology studies revealed that, in general, the surface morphology depended on the growth recipe and resulting thicknesses to some extent. In the case of ε-Fe_2O_3, Co_3O_4, ZrO_2 and HfO_2, grain-like features related to crystal growth covered the surfaces uniformly. However, the BiOCl nanoflakes in Fe_2O_3-BiOCl composites did not uniformly cover the uniform Fe_2O_3 layer, which might negatively influence the electrical properties of these samples. Due to the polycrystalline nature, the ZrO_2 layers in the ZrO_2-Al_2O_3 films cross-sectional studies appeared rather rough, and the irregularities increased as the number of constituent oxide growth cycles decreased. Quite expectedly, the distinction between different layers became more evident in the sample with slightly thicker Al_2O_3 and ZrO_2 constituent layers.

The possibility of depositing thin films to the inner regions of challenging 3D substrates was studied in selected samples because this is considered a precondition for several possible applications. The results demonstrated that the ε-Fe_2O_3 thin film and Er_2O_3:Fe_2O_3 mixed film could be successfully deposited to the inner regions of 3D substrates – the thin film reached the bottom of the 3D substrate and followed the shape of the substrate during deposition. The step coverage of 100 % was not achieved with the current, not separately optimized deposition parameters.

Most of the samples subjected to magnetic measurements demonstrated ferromagnetic-like behaviour at room temperature, although the characteristic parameters and properties varied noticeably. The ε-Fe_2O_3 containing specimens stood out from others in terms of several times higher coercivity, reaching up to ~10 kOe. The ε-Fe_2O_3 phase was the main contributor to the higher coercivity value of these samples. Annealing these Fe_2O_3-BiOCl composites resulted in noticeably reduced magnetic behaviour. Metastable phases and related defects induced considerable magnetization in materials not as commonly known for their magnetic properties – ZrO_2 and HfO_2. It was also noticed that the magnetization was somewhat better realized in the laminates or layered structures than in mixed films. Furthermore, the appearance of magnetization in the multilayer structures and nanolaminates supports the goal of depositing materials with multiferroic properties by combining magnetically and electrically polarizing thin films into one nanolaminate.

The electrical charge polarization in investigated samples was noticeably dominated or affected by interfacial polarization caused by leakage currents that enabled charge accumulation at oxide/electrode interfaces. Only the HfO_2-Al_2O_3 nanolaminate based stacks showed an apparent saturation of the charge values together with defined remnant polarization and coercivity characteristic to a ferroelectric material, indicating the contribution from ferroelectricity along with the leakage currents. The stabilization of the ferroelectric phase was possible thanks to the alternation of fully formed Al_2O_3 and HfO_2 layers, the formation of which could be confirmed by investigating the HRTEM cross-section images.

The resistive switching effect was not observed in the Fe_2O_3-BiOCl based stacks, which turned out to be moderately leaky. On the other hand, ZrO_2-Co_3O_4, ZrO_2-Al_2O_3, and HfO_2-Al_2O_3 nanolaminates based stacks demonstrated the resistive switching behaviour. The properties and extent of the resistive switching loops with their characteristic difference between high and low resistance states were affected by the composition and the order of the layers.

Thus, most of the composite films and nanolaminates deposited using the atomic layer deposition method showed ferromagnetic-like behaviour by demonstrating non-linear magnetization and hysteresis. Few materials behaved similarly to the ferroelectric material under the influence of an external electric field, and most of the samples demonstrated a resistive switching effect. The appearance of all three desired effects could be observed in HfO_2-Al_2O_3 nanolaminates. The ferroelectric component's contribution could not be completely ruled out also in other materials studied (for example, Er_2O_3-Fe_2O_3 and ZrO_2-Al_2O_3).

From a future perspective, coupling effects between magnetic and electric responses characteristic to multiferroic material should be investigated for these materials as such coupling was not studied yet. Further, due to the attractive magnetic and possibly multiferroic properties of ε-Fe_2O_3, it might be worth to continue experimenting by combining it with another potentially ferroelectric material into multilayer structures. For example, it would probably give us an attractive material if ε-Fe_2O_3 could be combined with the HfO_2 so that the HfO_2 ferroelectric metastable phase would remain present.

SUMMARY IN ESTONIAN

Magnetiliselt ja elektriliselt polariseeruvate õhukeste tahkiskilede aatomkihtsadestamine ja mikroskoopiline analüüs

Tänu materjalide ja tehnoloogia pidevale arengule on seadmed läinud mõõtudelt väiksemaks, kuid omadustelt funktsionaalsemaks. Selline seadmete miniatuurimine ja täiustamine ning uute lahenduste otsimine jätkub ka edaspidi, mistõttu püsib jätkuvalt nõudlus uudsete spetsiifiliste omadustega materjalide järele. Muuhulgas on huviorbiidis multiferroidsete omadustega või takistuslülituslikku efekti omavad õhukesed tahkiskiled, mida saaks tulevikus rakendada muuhulgas uue generatsiooni mäludes, näiteks multiferroidsetes või takistuslülituslikes muutmäludes. Ferromagnetismi ja ferroelektrilisuse kooseksisteerimine materjalis on siiski suhteliselt haruldane nähtus. Mistõttu on eriti tahkiskile kujul ja toatemperatuuril mõõdetavate multiferroidsete omadustega materjale tuvastatud vähe.

Selle töö eesmärgiks oli anda panus selliste uudsete materjalikombinatsioonide otsimisele ja karakteriseerimisele, mis võiksid näidata toatemperatuuril nii ferromagnetilist, ferroelektrilist kui ka takistuslülituslikku käitumist. Seda loodeti saavutada, liites potentsiaalselt ferromagnetiliste ja ferroelektriliste omadustega materjalid (peamiselt metalloksiidid) kokku mitmekihilistesse struktuuridesse ehk nanolaminaatidesse ja segukiledesse. Käesolevas dissertatsioonis sadestati aatomkihtsadestamise meetodit kasutades ZrO_2-Co_3O_4 nanolaminaadid, Fe_2O_3-BiOCl komposiidid, Er_2O_3-Fe_2O_3 segukiled ning ZrO_2-Al_2O_3 ja HfO_2-Al_2O_3 segukiled ja nanolaminaadid, seejärel karakteriseeriti neid struktuure. Töös kasutati õhukeste tahkiskilede ja nanolaminaatide valmistamiseks aatomkihtsadestamise meetodit, kuna see meetod võimaldab sadestada kõrgekvaliteedilisi ja kontrollitava paksusega õhukesi tahkiskilesid. Lisaks on see meetod praeguseks laialdaselt kasutuses mitmetes teadus- ja tööstuslikes rakendussuundades, sealhulgas mikroelektroonika valdkonnas.

Antud tööst selgus, et mitmetes sadestatud struktuurides õnnestus edukalt stabiliseerida metastabiilseid faase ning need faasid domineerisid faasikoostist mitmete sadestatud nanolaminaatide ja segukilede puhul. Näiteks täheldati suurenenud metastabiilsete polümorfide panust ZrO_2-Al_2O_3 ja HfO_2-Al_2O_3 kilestruktuurides. Lisaks õnnestus sadestuse tulemusena metastabiilse ε-Fe_2O_3 faasi stabiliseerimine, mis hiljem sadestamisjärgse lõõmutamise tagajärjel muutus stabiilseks α-Fe_2O_3 faasiks ehk hematiidiks. Sadestatud tahkiskilede pinna morfoloogia sõltus mõningal määral sadestusretseptist (ehk sadestustsüklite arvust ja vahekorrast) ning selle tulemusena sadestatud kihtide paksustest. Co_3O_4, ZrO_2, HfO_2 ja ε-Fe_2O_3 puhul oli pind ühtlaselt kaetud teraliste struktuuridega, mis on seostatavad kristallisatsiooniga. Kuid samas täheldati seda, et Fe_2O_3-BiOCl komposiitide koostisesse kuuluv BiOCl oli pinnale moodustunud nanoliistakutena. See nanoliistakute kiht ei katnud ühtlaselt selle all paiknevat ühtlase paksusega Fe_2O_3 kihti ning võib kaasa tuua selle, et need komposiidid on elektriliste mõõtmiste jaoks liiga lekkivad. Transmissioonelektronmikroskoobi abil ZrO_2-Al_2O_3 kilede läbilõikeid uurides selgus, et ZrO_2 kihid olid oma polükristallilise olemuse tõttu üsna karedad ehk ebatasased. Need ebatasasused eristusid selgemalt sellistes segukiledes, kus metalloksiidide sadestustsüklite arv oli väiksem. Ootuspäraselt eristusid Al_2O_3 ja ZrO_2 ühtlasemad kihid selgelt nanolaminaadis, mille kihid olid võrreldes teistega veidi paksemad.

Lisaks uuriti osade sadestatud proovide puhul õhukeste kilede sügavate ja kitsaste kanalitega 3D-aluse siseseintele sadestamise võimalikkust, kuna seda peetakse mitmete võimalike rakenduste jaoks vajalikuks omaduseks. Selgus, et ε-Fe_2O_3 õhukesesi tahkiskilesi ja Er_2O_3:Fe_2O_3 segukilesi saab tõepoolest edukalt 3D-aluse siseseintele sadestada – õhuke kile sadestus edukalt 3D-aluse siseseintele ja põhja ning järgis sadestamise ajal alusmaterjali kuju. Samas võis täheldada, et sadestatud kilekihi paksus 3D-aluse sügavamas osas vähenes ehk kile paksus ei olnud kogu 3D struktuuri ulatuses päris ühtlane. Kuid kuna sadestusparameetrid ei olnud 3D-alustesse sadestamise jaoks eraldi optimeeritud, siis võib täiendav sadestusparameetrite optimeerimine tulevikus aidata kile paksust ühtlustada.

Enamikus magnetmõõtmistesse valitud kilestruktuurides tuvastati toatemperatuuril läbiviidud mõõtmiste käigus ferromagnetilisele materjalile omast küllastusmagneetumust, jääkmagneetumust ja mõõdetavat koertsitiivsust. Selle magnetilise hüstereesi tekkimise peamised mõjutegurid varieerusid veidi erinevate sadestatud materjalide korral. Kordades suurema koertsitiivsuse poolest eristusid teistest selgelt ε-Fe_2O_3 sisaldavad komposiidid, mille puhul ulatus koertsitiivsuse väärtus ~ 10 kOe-ni. Nende Fe_2O_3-BiOCl komposiitide selline magnetiline käitumine oli võimalik tänu ε-Fe_2O_3 faasi olemasolule. Komposiitide lõõmutamise tulemusena vähenesid nende koertsitiivsus ja küllastusmagneetumus märgatavalt. Lisaks täheldati, et metastabiilsed faasid ja nendega kaasnevad defektid põhjustasid märkimisväärset magnetiseerumist materjalides, mis ei ole oma magnetiliste omaduste poolest niivõrd tuntud. Sellised materjalid olid näiteks ZrO_2 ja HfO_2. Märgati ka seda, et magneetumine oli nanolaminaatides võrreldes segukiledega mõnevõrra paremini realiseerunud. Üleüldiselt toetasid saadud tulemused ehk ferromagnetilise hüstereesi ilmnemine mitmekomponendilistes struktuurides ja nanolaminaatides eesmärki sadestada multiferroidsete omadustega materjale kombineerides selleks magnetiliselt ja elektriliselt polariseeruvaid õhukesi tahkiskilesid ühte kihtstruktuuri kokku.

Kilestruktuuride elektrilist polariseeritavust uurides selgus, et proovides domineeris märgatavalt piirpindade vaheline polarisatsioon, mida põhjustasid lekkevoolud, mis võimaldasid laengute kogunemist oksiidi/elektroodi piirpindadele. Ainult HfO_2-Al_2O_3 nanolaminaatidel baseeruvad struktuurid näitasid lisaks jääkpolarisatsioonile ja koertsitiivsusele ka ferroelektrilisele materjalile iseloomulikku selget laengu küllastumist, viidates lisaks lekkevoolude poolt põhjustatud polarisatsioonile ka ferroelektrilise komponendi olemasolule ja panusele. Metastabiilset ferroelektriliste omaduste poolest tuntud faasi oli neis nanolaminaatides võimalik stabiliseerida tänu sellele, et HfO_2 kihte eraldasid üksteisest piisavalt paksud ja terviklikult moodustunud Al_2O_3 kihid. Kihtide terviklikkust oli võimalik hinnata transmissioonelektronmikroskoobi abil.

Fe_2O_3-BiOCl struktuurid osutusid lekkivateks ja takistuslülituslikku efekti neis ei tuvastatud. Küll aga esines takistuslülituslikku efekti nii ZrO_2-Co_3O_4, ZrO_2-Al_2O_3 kui ka HfO_2-Al_2O_3 nanolaminaatides, kus sadestatud kihtide koostis ja järjestus mõjutasid takistuslülituslikke omadusi ja ulatust.

Seega võib öelda, et aatomkihtsadestamise meetodit kasutades sadestatud segukiledest ja nanolaminaatidest enamus käitusid ferromagnetilistele materjalidele sarnaselt polariseerudes välise magnetvälja mõjul. Neist osad käitusid ferroelektrilisele materjalile sarnaselt polariseerudes välise elektrivälja mõjul ja enamus uuritud katseobjektidest demonstreerisid takistuslülituslikus režiimis töötades takistuslülitusliku efekti olemasolu. HfO_2-Al_2O_3 nanolaminaatides täheldati kõigi kolme soovitud efekti esinemist, kuigi ka teistes uuritud materjalides (nt Er_2O_3-Fe_2O_3 ja ZrO_2-Al_2O_3) ei saanud ferroelektrilise komponendi olemasolu ja panust täielikult välistada.

Tulevikuperspektiivist lähtudes on järgmiseks oluliseks sammuks uurida nendes materjalides ferromagnetilise ja ferroelektrilise käitumise vahelist vastasmõju, kuna sellist vastastikmõju käesoleva töö käigus ei uuritud. Lisaks sellele võiks olla põhjendatud soovitus jätkata katsetusi selliste materjalikombinatsioonidega, kus üheks komponendiks oleks ε-Fe_2O_3 oma magnetiliste ja potentsiaalselt ka multiferroidsete omaduste tõttu ja teiseks komponendiks mõni teine potentsiaalselt ferroelektriliste omadustega materjal. Näiteks võiks anda soovitud atraktiivse multiferroidse või magnetoelektrilise materjali selline olukord, kus õnnestuks ε-Fe_2O_3 edukalt kombineerida HfO_2-ga selliselt, et HfO_2 kihis säiliks ferroelektriline metastabiilne faas.

ACKNOWLEDGEMENTS

I would like to express my heartfelt gratitude to my supervisors Dr. Aile Tamm and Prof. Kaupo Kukli, for their advice, support, guidance, wise words and useful discussions over the years, starting already from the end of my bachelor studies. I am grateful to them for all the self-development opportunities they directed me to or made possible and for always being there for me when advice or feedback was necessary.

I am also very grateful to Dr. Jekaterina Kozlova for her patience and for sharing her valuable knowledge and expertise related to lamella creation and electron microscopy over the years, starting with teaching fundamental SEM competence to me at the end of my bachelor studies. I would also like to thank Prof. Väino Sammelselg for the access to operating the SEM-FIB device independently and Dr. Mihkel Rähn for TEM related analysis and support.

I wish to thank Dr. Taivo Jõgiaas for inviting me to the Laboratory of Thin Film Technology to work on my bachelor thesis and teaching the technical aspects of our laboratory ALD reactors. I am thankful to Mr. Peeter Ritslaid for sharing his expertise related to XRF, Mrs. Alma-Asta Kiisler for the help with pre-deposition substrate cleaning activities, Dr. Kristjan Kalam and our collaboration partners Dr. Raivo Stern, Mr. Joosep Link, Prof. Salvador Dueñas and Prof. Helena Castán for their support and successful collaboration over the years. I am also profoundly grateful to all the co-authors for their contribution to the publications and additional support. All the colleagues from the Laboratory of Thin Film Technology are sincerely thanked for their help and discussions.

I am immensely grateful to my parents Heli and Kalev, and my husband-to-be Mihkel, for their understanding, support and patience during my studies and for always believing in me. I am also thankful to my closest friends, relatives and co-workers from KSVEE for their supportive conversations and understanding.

REFERENCES

[1] A. K. Petford-Long, A. N. Chiaramonti, Transmission electron microscopy of multilayer thin films, *Annual Review of Materials Research* 38 (2008) 559–584.

[2] D.-H. Kwon, K. M. Kim, J. H. Jang, J. M. Jeon, M. H. Lee, G. H. Kim, X.-S. Li, G.-S. Park, B. Lee, S. Han, M. Kim, C. S. Hwang, Atomic structure of conducting nanofilaments in TiO_2 resistive switching memory, *Nature Nanotechnology* 5 (2010) 148–153.

[3] A. Sawa, Resistive switching in transition metal oxides, *Materials Today* 11 (2008) 28–36.

[4] F. Pan, S. Gao, C. Chen, C. Song, F. Zeng, Recent progress in resistive random access memories: Materials, switching mechanisms, and performance, *Materials Science and Engineering: R: Reports* 83 (2014) 1–59.

[5] S. Slesazeck, T. Mikolajick, Nanoscale resistive switching memory devices: a review, *Nanotechnology* 30 (2019) 352003.

[6] T.-C. Chang, K.-C. Chang, T.-M. Tsai, T.-J. Chu, S. M. Sze, Resistance random access memory, *Materials Today* 19 (2016) 254–264.

[7] D. Khomskii, Classifying multiferroics: Mechanisms and effects, *Physics* 2 (2009) 20.

[8] L. W. Martin, Y.-H. Chu, R. Ramesh, Advances in the growth and characterization of magnetic, ferroelectric, and multiferroic oxide thin films, *Materials Science and Engineering: R: Reports* 68 (2010) 89–133.

[9] W. Eerenstein, N. D. Mathur, J. F. Scott, Multiferroic and magnetoelectric materials, *Nature* 442 (2006) 759–765.

[10] J. Wang, J. B. Neaton, H. Zheng, V. Nagarajan, S. B. Ogale, B. Liu, D. Viehland, V. Vaithyanathan, D. G. Schlom, U. V. Waghmare, N. A. Spaldin, K. M. Rabe, M. Wuttig, R. Ramesh, Epitaxial $BiFeO_3$ multiferroic thin film heterostructures, *Science* 299 (2003) 1719–1722.

[11] L. W. Martin, S. P. Crane, Y.-H. Chu, M. B. Holcomb, M. Gajek, M. Huijben, C.-H. Yang, N. Balke, R. Ramesh Martin, Multiferroics and magnetoelectrics: thin films and nanostructures, *J. Phys.: Condens. Matter* 20 (2008) 434220.

[12] P. B. Meisenheimer, S. Novakov, N. M. Vu, J. T. Heron, Perspective: Magnetoelectric switching in thin film multiferroic heterostructures, *Journal of Applied Physics* 123 (2018) 240901.

[13] W. Li, J. Shi, K. H. L. Zhang, J. L. MacManus-Driscoll, Defects in complex oxide thin films for electronics and energy applications: challenges and opportunities, *Mater. Horiz.* 7 (2020) 2832–2859.

[14] G. M. De Luca, D. Preziosi, F. Chiarella, R. Di Capua,S. Gariglio, S. Lettieri, M. Salluzzo, Ferromagnetism and ferroelectricity in epitaxial $BiMnO_3$ ultra-thin films, *Appl. Phys. Lett.* 103 (2013) 062902.

[15] E.-M. Choi, T. Maity, A. Kursumovic, P. Lu, Z. Bi, S. Yu, Y. Park, B. Zhu, R. Wu, V. Gopalan, H. Wang, J. L. MacManus-Driscoll, Nanoengineering room temperature ferroelectricity into orthorhombic $SmMnO_3$ films, *Nature Communications* 11 (2020) 2207.

[16] Z. Hu, X. Wang, T. Nan, Z. Zhou, B. Ma, X. Chen, J. G. Jones, B. M. Howe, G. J. Brown, Y. Gao, H. Lin, Z. Wang, R. Guo, S. Chen, X. Shi, W. Shi, H. Sun, D. Budil, M. Liu, N. X. Sun, Non-volatile ferroelectric switching of ferromagnetic resonance in NiFe/PLZT multiferroic thin film heterostructures, *Scientific Reports* 6 (2016) 32408.

[17] S.-O. Hwang, Y. J. Eum, J.-W. Kim, J. Ryu, C. Y. Koo, J.-Y. Lee, H. Y. Lee, Magnetoelectric coupling effect in ferroelectric and ferromagnetic hybrid thin films, *Integrated Ferroelectrics* 157 (2014) 57–62.

[18] S. Ren, G. Zhu, J. Xie, J. Bu, H. Qin, J. Hu, Resistive switching and electrical control of ferromagnetism in a Ag/HfO_2/Nb:$SrTiO_3$/Ag resistive random access memory (RRAM) device at room temperature, *J. Phys.: Condens. Matter* 28 (2016) 056001.

[19] I. Alposta, A. Kalstein, N. Ghenzi, S. Bengio, G. Zampieri, D. Rubi, P. Levy, Resistive switching in ferromagnetic $La_{2/3}Ca_{1/3}MnO_3$ thin films, *IEEE Transactions on Magnetics* 49 (2013) 4582–4585.

[20] M.-C. Kao, H.-Z. Chen, S.-L. Young, K.-H. Chen, J.-L. Chiang, J.-B. Shi, Structural, electrical, magnetic and resistive switching properties of the multiferroic/ferroelectric bilayer thin films, *Materials* 10 (2017) 1327.

[21] M. G. A. Ranieri, P. P. Ortega, H. Moreno, M. A. Ramirez, E. C. Aguiar, A. Z. Simōes, Resistive switching and multiferroic behavior of $La_{0.5}Pr_{0.5}FeO_3$ ferrite thin films, *Journal of Alloys and Compounds* 851 (2021) 156936.

[22] M. Sezen, "Focused Ion Beams (FIB) – Novel methodologies and recent applications for multidisciplinary sciences," in *Modern Electron Microscopy in Physical and Life Sciences*, M. Janecek, R. Kral, eds. (IntechOpen, 2016), 121–140.

[23] A. Tanskanen, O. Mustonen, M. Karppinen, Simple ALD process for ε-Fe_2O_3 thin films, *APL Materials* 5 (2017) 056104.

[24] A. A. Dubrovskiy, D. A. Balaev, K. A. Shaykhutdinov, O. A. Bayukov, O. N. Pletnev, S. S. Yakushkin, G. A. Bukhtiyarova, O. N. Martyanov, Size effects in the magnetic properties of ε-Fe_2O_3 nanoparticles, *Journal of Applied Physics* 118 (2015) 213901.

[25] M. Gich, I. Fina, A. Morelli, F. Sánchez, M. Alexe, J. Gàzquez, J. Fontcuberta, A. Roig, Multiferroic iron oxide thin films at room temperature, *Advanced Materials* 26 (2014) 4645–4652.

[26] J. Müller, P. Polakowski, S. Müller, T. Mikolajick, (Invited) Ferroelectric hafnium oxide based materials and devices: assessment of current status and future prospects. *ECS Trans.* 64 (2014) 159.

[27] P. Polakowski, J. Müller, Ferroelectricity in undoped hafnium oxide, *Appl. Phys. Lett.* 106 (2015) 232905.

[28] T. Ali, P. Polakowski, S. Riedel, T. Büttner, T. Kämpfe, M. Rudolph, B. Pätzold, K. Seidel, D. Löhr, R. Hoffmann, M. Czernohorsky, K. Kühnel, X. Thrun, N. Hanisch, P. Steinke, J. Calvo, J. Müller, Silicon doped hafnium oxide (HSO) and hafnium zirconium oxide (HZO) based FeFET: A material relation to device physics, *Appl. Phys. Lett.* 112 (2018) 222903.

[29] S. L. Weeks, A. Pal, V. K. Narasimhan, K. A. Littau, T. Chiang, Engineering of ferroelectric HfO_2–ZrO_2 nanolaminates, *ACS Appl. Mater. Interfaces* 9 (2017) 13440–13447.

[30] X. Tian, S. Shibayama, T. Nishimura, T. Yajima, S. Migita, A. Toriumi, Evolution of ferroelectric HfO_2 in ultrathin region down to 3 nm, *Appl. Phys. Lett.* 112 (2018) 102902.

[31] S. Eränen, "Thin Films on Silicon," in *Handbook of Silicon Based MEMS Materials and Technologies*, M. Tilli, T. Motooka, V.-M. Airaksinen, S. Franssila, M. Paulasto-Kröckel, V. Lindroos, eds. (William Andrew Publishing, 2015) 124–205.

[32] R. W. Johnson, A. Hultqvist, S. F. Bent, A brief review of atomic layer deposition: from fundamentals to applications, *Materials Today* 17 (2014) 236–246.

[33] M. Ritala, J. Niinistö, Industrial applications of atomic layer deposition, *ECS Trans.* 25 (2009) 641.

[34] M. Leskelä, M. Mattinen, M. Ritala, Review Article: Atomic layer deposition of optoelectronic materials, *Journal of Vacuum Science & Technology* B 37 (2019) 030801.

[35] V. Dias, H. Maciel, M. Fraga, A. Lobo, R. Pessoa, F. Marciano, Atomic layer deposited TiO_2 and Al_2O_3 thin films as coatings for aluminum food packaging application, Materials 12 (2019) 682.

[36] E. Marin, A. Lanzutti, L. Fedrizzi, Tribological properties of nanometric atomic layer depositions applied on AISI 420 stainless steel, *Tribology in Industry* 35 (2013) 208-216.

[37] D. Muñoz-Rojas, T. Maindron, A. Esteve, F. Piallat, J.C.S. Kools, J.-M. Decams, Speeding up the unique assets of atomic layer deposition, *Materials Today Chemistry* 12 (2019) 96–120.

[38] S. A. Skoog, J. W. Elam, R. J. Narayan, Atomic layer deposition: medical and biological applications, *International Materials Reviews* 58 (2013) 113–129.

[39] O. Graniel, M. Weber, S. Balme, P. Miele, M. Bechelany, Atomic layer deposition for biosensing applications, *Biosensors and Bioelectronics* 122 (2018) 147–159.

[40] R. L. Puurunen, Surface chemistry of atomic layer deposition: A case study for the trimethylaluminum/water process, *J. Appl. Phys.* 97 (2005) 121301.

[41] M. Leskelä, M. Ritala, Atomic layer deposition chemistry: recent developments and future challenges, *Angewandte Chemie International Edition* 42 (2003) 5548–5554.

[42] M. Leskelä, M. Ritala, Atomic layer deposition (ALD): from precursors to thin film structures, *Thin Solid Films* 409 (2002) 138–146.

[43] T. Suntola, Atomic layer epitaxy, *Materials Science Reports* 4 (1989) 261–312.

[44] Y. Zhang, M. Liu, Y. Zhang, X.Chen, W. Ren, Z.-G. Ye, Atomic layer deposition of superparamagnetic and ferrimagnetic magnetite thin films, *Journal of Applied Physics* 117 (2015) 17C743.

[45] K. Kukli, J. Ihanus, M. Ritala, M. Leskela, Tailoring the dielectric properties of HfO_2–Ta_2O_5 nanolaminates, *Appl. Phys. Lett.* 68 (1996) 3737–3739.

[46] S.-H. K. Park, J. Oh, C.-S. Hwang, J.-I. Lee, Y. S. Yang, H. Y. Chu, Ultrathin film encapsulation of an OLED by ALD, *Electrochem. Solid-State Lett.* 8 (2005) H21.

[47] Y. Yong-Qiang, D. Yu, Optimization of Al_2O_3 films deposited by ALD at low temperatures for OLED encapsulation, *J. Phys. Chem. C* 118 (2014) 18783–18787.

[48] J. Kostamo, T. Malinen, V. Sammelselg, J. Aarik L. Aarik, Protecting an interior of a hollow body with an ald coating, PCT/FI2014/050153 (3.03.2014).

[49] V. Sammelselg, L. Aarik, M. Merisalu, Method of preparing corrosion resistant coatings, UK1223532.1 (31.12.2012).

[50] V. Sammelselg, J. Kostamo, W. Bayerl, J. Aarik, L. Aarik, S. Lindfors, P. Adam, J. Poutiainen, Protecting an interior of a gas container with an ALD coating, WO 2015/1324443 A1 (3.03.2014).

[51] J. Maula, Atomic layer deposition for industrial optical coatings, *Chinese Optics Letters* 8 (2010) 53–58.

[52] V. Cremers, R. L. Puurunen, J. Dendooven, Conformality in atomic layer deposition: Current status overview of analysis and modelling, Applied Physics Reviews 6 (2019) 021302.

[53] D. Arenas-Lago, A. Rodríguez-Seijo, L. Andrade Couce, F. A. Vega, "A Multianalytical Approach for the Assessment of Toxic Element Distribution in Soils From Mine and Quarry Areas," in *Assessment, Restoration and Reclamation of Mining Influenced Soils*, J. Bech, C. Bini, M. A. Pashkevich, eds. (Academic Press, 2017) 33–62.

[54] K. D. Vernon-Parry, Scanning electron microscopy: an introduction, *III-Vs Review* 13 (2000) 40–44.

[55] J. I. Goldstein, D. E. Newbury, J. R. Michael, N. W. M. Ritchie, J. H. J. Scott, D. C. Joy, *Scanning Electron Microscopy and X-Ray Microanalysis* (Springer, 2018).

[56] W. Zhou, Z. L. Wang, *Scanning Microscopy for Nanotechnology: Techniques and Applications* (Springer, 2007).

[57] R. F. Egerton, *Physical principles of electron microscopy* (Springer, 2005).

[58] J. Mayer, L. A. Giannuzzi, T. Kamino, J. Michael, TEM sample preparation and FIB-induced damage, *MRS Bulletin* 32 (2007) 400–407.

[59] L. A. Giannuzzi, F. A. Stevie, *Introduction to Focused Ion Beams: Instrumentation, Theory, Techniques and Practice* (Springer, 2005).

[60] S. Abolhassani, S. P. Gasser, Preparation of TEM samples of metal–oxide interface by the focused ion beam technique, *Journal of Microscopy* 223 (2006) 73–82.

[61] K. Song, "Interphase characterization in rubber nanocomposites," in *Progress in Rubber Nanocomposites*, S. Thomas, H. J. Maria, eds. (Woodhead Publishing, 2017) 115–152.

[62] Z. Luo, *A Practical Guide to Transmission Electron Microscopy: Fundamentals* (Momentum Press, New York, 2016).

[63] T. Arroval, L. Aarik, R. Rammula, V. Kruusla, J. Aarik, Effect of substrate-enhanced and inhibited growth on atomic layer deposition and properties of aluminum–titanium oxide films, *Thin Solid Films* 600 (2016) 119–125.

[64] T. Suntola, Atomic layer epitaxy, *Thin Solid Films* 216 (1992) 84–89.

[65] S. Y. Lee, H. K. Kim, J. H. Lee, I.-H. Yu, J.-H. Lee, C. S. Hwang, Effects of O_3 and H_2O as oxygen sources on the atomic layer deposition of HfO_2 gate dielectrics at different deposition temperatures, *J. Mater. Chem. C* 2 (2014) 2558–2568.

[66] T. Kondo, Y. Sawada, H. Funakubo, K. Akiyama, T. Kiguchi, M. Wang, T. Uchida, Good conformability of indium-tin oxide thin films prepared by spray chemical vapor deposition, *Electrochem. Solid-State Lett.* 12 (2009) D42.

[67] A. Tamm, A. Tarre, V. Verchenko, H. Seemen, R. Stern, Atomic layer deposition of superconducting CuO thin films on three-dimensional substrates, *Crystals* 10 (2020) 650.

[68] B. Sun, W. Zhao, Y. Xiong, Y. Lin, P. Chen, Effect of thickness and annealing temperature on magnetic properties of ultrathin γ-Fe_2O_3 films grown on silicon substrate, *Metall Mater Trans A* 45 (2014) 5245–5248.

[69] U. Klekotka, D. Satuła, B. Kalska-Szostko, ε-phase of iron oxide out of thermally treated magnetite nanoparticles, *Journal of Magnetism and Magnetic Materials* 497 (2020) 165999.

[70] M. Rozana, K. A. Razak, C. K. Yew, Z. Lockman, Rozana, Annealing temperature-dependent crystallinity and photocurrent response of anodic nanoporous iron oxide film, *Journal of Materials Research* 31 (2016) 1681–1690.

[71] A. A. Putri, S. Kato, N. Kishi, T. Soga, Study of annealing temperature effect on the photovoltaic performance of BiOI-based materials, *Applied Sciences* 9 (2019) 3342.

[72] X. Liu, Y. Su, Q. Zhao, C. Du, Z. Liu, Constructing $Bi_{24}O_{31}Cl_{10}$/BiOCl heterojunction via a simple thermal annealing route for achieving enhanced photocatalytic activity and selectivity, *Scientific Reports* 6 (2016) 28689.

[73] E. Çetinörgü-Goldenberg, J.-E. Klemberg-Sapieha, L. Martinu, Effect of post-deposition annealing on the structure, composition, and the mechanical and optical characteristics of niobium and tantalum oxide films, *Appl. Opt.* 51 (2012) 6498–6507.

[74] S. Won, S. Go, W. Lee, K. Jeong, H. Jung, C. Lee, E. Lee, J. Lee, Effects of defects generated in ALD TiO_2 films on electrical properties and interfacial reaction in TiO_2/SiO_2/Si system upon annealing in vacuum, *Met. Mater. Int.* 14 (2008) 759–765.

[75] N. Nikolaou, P. Dimitrakis, P. Normand, D. Skarlatos, K. Giannakopoulos, K. Mergia, V. Ioannou-Sougleridis, K. Kukli, J. Niinistö, K. Mizohata, M. Ritala, M. Leskelä, Inert ambient annealing effect on MANOS capacitor memory characteristics, *Nanotechnology* 26 (2015) 134004.

[76] Y. Makimizu, J. Yoo, M. Poornajar, N. T. Nguyen, H.-J. Ahn, I. Hwang, S. Kment, P. Schmuki, Effects of low oxygen annealing on the photoelectrochemical water splitting properties of α-Fe_2O_3, *J. Mater. Chem. A* 8 (2020) 1315–1325.

[77] I. S. Golovina, M. Falmbigl, A. V. Plokhikh, T. C. Parker, C. Johnson, J. E. Spanier, Effect of annealing conditions on the electrical properties of ALD-grown polycrystalline $BiFeO_3$ films, *J. Mater. Chem. C* 6 (2018) 5462–5472.

[78] B. J. Choi, D. S. Jeong, S. K. Kim, C. Rohde, S. Choi, J. H. Oh, H. J. Kim, C. S. Hwang, K. Szot, R. Waser, B. Reichenberg, and S. Tiedke, Resistive switching mechanism of TiO_2 thin films grown by atomic-layer deposition, *Journal of Applied Physics* 98 (2005) 033715.

[79] K. M. Kim, D. S. Jeong, C. S. Hwang, Nanofilamentary resistive switching in binary oxide system; a review on the present status and outlook, *Nanotechnology* 22 (2011) 254002.

[80] E. Ambrosi, A. Bricalli, M. Laudato, D. Ielmini, Impact of oxide and electrode materials on the switching characteristics of oxide ReRAM devices, *Faraday Discuss.* 213 (2019) 87–98.

[81] S. Ren, H. Qin, J. Bu, G. Zhu, J. Xie, J. Hu, Coexistence of electric field controlled ferromagnetism and resistive switching for TiO_2 film at room temperature, *Appl. Phys. Lett.* 107 (2015) 062404.

[82] I. Valov, Interfacial interactions and their impact on redox-based resistive switching memories (ReRAMs), *Semicond. Sci. Technol.* 32 (2017) 093006.

[83] S. C. Das, A. Shahee, N. P. Lalla, T. Shripathi, A simple and low cost Sawyer-Tower ferro-electric loop tracer with variable frequency and compensation circuit, *Proceedings of the 54th DAE Solid State Physics Symposium* 54 (2009) 439–440.

[84] M. Gich, J. Gazquez, A. Roig, A. Crespi, J. Fontcuberta, J. C. Idrobo, S. J. Pennycook, M. Varela, V. Skumryev, M. Varela, Epitaxial stabilization of ε-Fe_2O_3 (00l) thin films on $SrTiO_3$ (111), *Appl. Phys. Lett.* 96 (2010) 112508.

[85] S. S. Kulkarni, C. D. Lokhande, Structural, optical, electrical and dielectrical properties of electrosynthesized nanocrystalline iron oxide thin films, *Materials Chemistry and Physics* 82 (2003) 151–156.

[86] J. Tuček, R. Zbořil, A. Namai, S. Ohkoshi, ε-Fe_2O_3: An advanced nanomaterial exhibiting giant coercive field, millimeter-wave ferromagnetic resonance, and magnetoelectric coupling, *Chem. Mater.* 22 (2010) 6483–6505.

[87] R. Zboril, M. Mashlan, K. Barcova, M. Vujtek, Thermally induced solid-state syntheses of γ-Fe_2O_3 nanoparticles and their transformation to α-Fe_2O_3 via ε-Fe_2O_3, *Hyperfine Interactions* 139 (2002) 597–606.

[88] E. Tronc, C. Chanéac, J. P. Jolivet, Structural and magnetic characterization of ε-Fe_2O_3, *Journal of Solid State Chemistry* 139 (1998) 93–104.

[89] R. Ramesh, N. A. Spaldin, Multiferroics: progress and prospects in thin films, *Nature Materials* 6 (2007) 21–29.

[90] D. L. Leslie-Pelecky, R. D. Rieke, Magnetic properties of nanostructured materials, *Chem. Mater.* 8 (1996) 1770–1783.

[91] R. Singh, Unexpected magnetism in nanomaterials, *Journal of Magnetism and Magnetic Materials* 346 (2013) 58–73.

[92] G. C. Papaefthymiou, Nanoparticle magnetism, *Nano Today* 4 (2009) 438–447.

[93] D.-S. Park, A. D. Rata, I. V. Maznichenko, S. Ostanin, Y. L. Gan, S. Agrestini, G. J. Rees, M. Walker, J. Li, J. Herrero-Martin, G. Singh, Z. Luo, A. Bhatnagar, Y. Z. Chen, V. Tileli, P. Muralt, A. Kalaboukhov, I. Mertig, K. Dörr, A. Ernst, N. Pryds, The emergence of magnetic ordering at complex oxide interfaces tuned by defects, *Nature Communications* 11 (2020) 3650.

[94] M. Venkatesan, C. B. Fitzgerald, J. M. D. Coey, Unexpected magnetism in a dielectric oxide, *Nature* 430 (2004) 630–630.

[95] N. H. Hong, Magnetism due to defects/oxygen vacancies in HfO_2 thin films, *physica status solidi (c)* 4 (2007) 1270–1275.

[96] O. E. Tereshchenko, V. A. Golyashov, S. V. Eremeev, I. Maurin, A. V. Bakulin, S. E. Kulkova, M. S. Aksenov, V. V. Preobrazhenskii, M. A. Putyato, B. R. Semyagin, D. V. Dmitriev, A. I. Toropov, A. K. Gutakovskii, S. E. Khandarkhaeva, I. P. Prosvirin, A. V. Kalinkin, V. I. Bukhtiyarov, A. V. Latyshev, Ferromagnetic HfO_2/Si/GaAs interface for spin-polarimetry applications, *Appl. Phys. Lett.* 107 (2015) 123506.

[97] K. K. Bharathi, S. Venkatesh, G. Prathiba, N. H. Kumar, C. V. Ramana, Room temperature ferromagnetism in HfO_2 films, *Journal of Applied Physics* 109 (2011) 07C318.

[98] J. M. D. Coey, M. Venkatesan, P. Stamenov, C. B. Fitzgerald, L. S. Dorneles, Magnetism in hafnium dioxide, *Phys. Rev. B* 72 (2005) 024450.

[99] K. Kukli, M. C. Dimri, A. Tamm, M. Kemell, T. Käämbre, M. Vehkamäki, M. Puttaswamy, R. Stern, I. Kuusik, A. Kikas, M. Tallarida, D. Schmeißer, M. Ritala, M. Leskelä, Structural and magnetic studies on iron oxide and iron-magnesium oxide thin films deposited using ferrocene and (dimethylaminomethyl)ferrocene precursors, *ECS J. Solid State Sci. Technol.* 2 (2012) N45.

[100] M. Puttaswamy, M. Vehkamäki, K. Kukli, M. C. Dimri, M. Kemell, T. Hatanpää, M. J. Heikkilä, K. Mizohata, R. Stern, M. Ritala, M. Leskelä, Bismuth iron

oxide thin films using atomic layer deposition of alternating bismuth oxide and iron oxide layers, *Thin Solid Films* 611 (2016) 78–87.

[101] F. Máca, J. Kudrnovský, V. Drchal, G. Bouzerar, Magnetism without magnetic impurities in ZrO_2 oxide, *Appl. Phys. Lett.* 92 (2008) 212503.

[102] S. Ning, P. Zhan, Q. Xie, Z. Li, Z. Zhang, Room-temperature ferromagnetism in un-doped ZrO_2 thin films, *J. Phys. D: Appl. Phys.* 46 (2013) 445004.

[103] M. A. Rahman, S. Rout, J. P. Thomas, D. McGillivray, K. T. Leung, Defect-rich dopant-free ZrO_2 nanostructures with superior dilute ferromagnetic semiconductor properties, *J. Am. Chem. Soc.* 138 (2016) 11896–11906.

[104] S. Ning, Z. Zhang, Phase-dependent and defect-driven d0 ferromagnetism in undoped ZrO_2 thin films, *RSC Adv.* 5 (2014) 3636–3641.

[105] G. Bouzerar, T. Ziman, Model for vacancy-induced d0 ferromagnetism in oxide compounds, *Phys Rev Lett* 96 (2006) 207602.

[106] Y. Wang, W. Chen, B. Wang, Y. Zheng, Ultrathin ferroelectric films: growth, characterization, physics and applications, *Materials* 7 (2014) 6377–6485.

[107] K. A. Hunnestad, E. D. Roede, A. T. J. van Helvoort, D. Meier, Characterization of ferroelectric domain walls by scanning electron microscopy, *Journal of Applied Physics* 128 (2020) 191102.

[108] M. Hoffmann, P. V. Ravindran, A. I. Khan, Why do ferroelectrics exhibit negative capacitance?, *Materials* 12 (2019) 3743.

[109] J. F. Scott, Ferroelectrics go bananas, *J. Phys.: Condens. Matter* 20 (2008) 021001.

[110] A. K. Tagantsev, Mechanisms of polarization switching in ferroelectric thin films, *Ferroelectrics* 184 (1996) 79–88.

[111] N. I. Lebedev, A. S. Sigov, Surface inhomogeneities and coercive field of thin ferroelectric films, *Integrated Ferroelectrics* 4 (1994) 21–24.

[112] H. Yokota, T. Nozue, S. Nakamura, H. Hojo, M. Fukunaga, P.-E. Janolin, J.-M. Kiat, A. Fuwa, Ferroelectricity and weak ferromagnetism of hexagonal $ErFeO_3$ thin films, *Phys. Rev. B* 92 (2015) 054101.

PUBLICATIONS

CURRICULUM VITAE

Name: Helina Seemen
Date of Birth: 26.04.1993
E-mail: helina.seemen@ut.ee, helinaseemen@gmail.com

Education

2017–…	University of Tartu, Doctor of Philosophy, Materials Science
2015–2017	University of Tartu, Master of Science, Materials Science
2012–2015	University of Tartu, Bachelor of Science, Physics
2009–2012	Rakvere Private Gymnasium (*cum laude*)

Work experience

01.08.2019–...	Karl Storz Video Endoscopy Estonia OÜ, validation engineer (1,00)
18.10.2018–30.06.2019	University of Tartu, Faculty of Science and Technology, Institute of Physics, specialist (0,60)
01.05.2018–30.06.2018	University of Tartu, Faculty of Science and Technology, Institute of Physics, engineer (0,60)
01.09.2017–30.04.2018	University of Tartu, Faculty of Science and Technology, Institute of Physics, engineer (working under additional scholarship)
01.01.2016–30.06.2017	University of Tartu, Faculty of Science and Technology, Institute of Physics, engineer (0,40)
01.07.2015–31.12.2015	University of Tartu, Faculty of Science and Technology, Institute of Physics, University of Tartu, engineer (0,40)
01.10.2014–30.06.2015	University of Tartu, Faculty of Science and Technology, Institute of Physics, University of Tartu, Laboratory Assistant (0,30)

Publications

A total of 18 scientific articles are listed in the “List of original publications and author’s contributions” and “List of author’s other publications” chapters of the Thesis. Visit https://www.etis.ee/CV/Helina_Seemen/eng for additional and up-to-date information.

Presentations at conferences

Oral presentations for which I was presenting author:

1. **H. Seemen**, K. Kukli, A. Tamm, Properties of atomic layer deposited ZrO_2 or Fe_2O_3 based multilayers, AVS 21st International Conference on Atomic Layer Deposition (ALD 2021), 27.06.–30.06.2021, virtual meeting, virtual on-demand oral presentation.
2. **H. Seemen**, K. Kukli, A. Tamm, Magnetic properties of atomic layer deposited multilayer thin solid films, GSFMT Scientific Conference 2021, 14.06.–15.06.2021, Tartu (Estonia), virtual presentation.

3. **H. Seemen**, J. Link, R. Stern, T. Jõgiaas, K. Kukli, A. Tamm, Properties of atomic layer deposited iron and bismuth oxide layered structures, GSFMT Scientific Conference 2019, 04.02.–05.02.2019, Tartu (Estonia).
4. **H. Seemen**, M. Rähn, K. Kalam, T. Sajavaara, S. Dueñas, H. Castán, J. Link, R. Stern, K. Kukli, A. Tamm, Properties of atomic layer deposited zirconium and cobalt oxide nanolaminates, 12th International Scientific Conference on Functional Materials and Nanotechnologies – FM&NT 2018, 02.10.–05.10.2018, Riga (Latvia).
5. **H. Seemen**, M. Rähn, K. Kalam, T. Sajavaara, S. Dueñas, H. Castán, J. Link, R. Stern, K. Kukli, A. Tamm, Defect-induced effects in atomic layer deposited zirconium and cobalt oxide nanolaminates, The 2018 E-MRS Spring Meeting and Exhibit, 18.06.–22.06.2018, Strasbourg (France), invited talk.

Poster presentations for which I was presenting author:

1. **H. Seemen**, M. Rähn, T. Jõgiaas, J. Link, R. Stern, S. Dueñas, H. Castán, K. Kukli, A. Tamm, The importance of microscopic analysis on atomic layer deposited thin solid films, GSFMT Scientific Conference 2020, 04.02.–05.02.2020, Tallinn (Estonia).
2. **H. Seemen,** S. Dueñas, H. Castán, J. Link, R. Stern, T. Jõgiaas, K. Kukli, A. Tamm, Magnetic and electrical properties of atomic layer deposited iron oxide and bismuth oxide chloride layered structures, EuroCVD 22 – Baltic ALD 16 Conference, 24.06.–28.06.2019, Luxembourg (Luxembourg).
3. **H. Seemen,** M. Rähn, K. Kalam, S. Dueñas, H. Castán, J. Link, R. Stern, K. Kukli, A. Tamm, The properties of atomic layer deposited zirconium and cobalt oxide nanolaminates, GSFMT Scientific Conference 2018, 07.03.–08.03.2018, Tallinn (Estonia).
4. **H. Seemen,** K. Kalam, J. Kozlova, M. Rähn, V. Sammelselg, K. Kukli, A. Tamm, Using focused ion beam and transmission electron microscopy for examining thin film structures, Joint EUROCVD 21 – Baltic ALD 15 Conference, 11.06.–14.06.2017, Linköping (Sweden).
5. **H. Seemen,** T. Jõgiaas, A. Tamm, V. Sammelselg, The formation and distribution of cracks in bent atomic layer deposited coatings, ALD 2016 – the 16th International Conference on Atomic Layer Deposition, 24.07.–27.07.2016, Dublin (Ireland).
6. **H. Seemen,** T. Jõgiaas, R.-T. Kibur, Using atomic layer deposition for microtome blade cutting performance enhancement, The 13th International Baltic Conference on Atomic Layer Deposition – Baltic ALD 2015, 28.09.–29.09.2015, Tartu (Estonia).

Oral and poster presentations to which I contributed as a co-author:

1. K. Kalam, **H. Seemen**, M. Mikkor, T. Jõgiaas, P. Ritslaid, K. Kukli, A. Tamm, A. Kasikov, J. Link, R. Stern, S. Dueñas, H. Castán, Atomic layer deposition of ZrO_2-based thin films, GSFMT Scientific Conference 2020, 04.02.–05.02.2020, Tallinn (Estonia).

2. A. Tamm, A. Tarre, **H. Seemen**, K. Kukli, J. Link, R. Stern, Cupric oxide thin films grown by atomic layer deposition, EuroCVD 22 – Baltic ALD 16 Conference, 24.06.–28.06.2019, Luxembourg (Luxembourg).
3. K. Kukli, M. Kemell, M. J. Heikkilä, **H. Seemen**, K. Kalam, A. Tamm, H. Castán, S. Dueñas, J. Link, R. Stern, M. Ritala, M. Leskelä, Atomic layer deposition of metal oxide nanolaminates exhibiting nonlinear electrical and magnetic polarization with tunable resistivity, EuroCVD 22 – Baltic ALD 16 Conference, 24.06.–28.06.2019, Luxembourg (Luxembourg).
4. Ó. G. Ossorio, S. Dueñas, H. Castán, A. Tamm, K. Kalam, **H. Seemen**, K. Kukli, Resistive switching properties of atomic layer deposited ZrO_2-HfO_2 thin films, The 12th Spanish Conference on Electron Devices (CDE 2018), 14.11.–16.11.2018, Salamanca (Spain).
5. M. Mikkor, A. Šutka, **H. Seemen**, J. Merisalu, J. Link, R. Stern, S. Dueñas, H. Castán, K. Kukli, A. Tamm, Characterization of Bi_2O_3 film in compound with $MnFe_2O_3$ nanoparticles, 12th International Scientific Conference on Functional Materials and Nanotechnologies – FM&NT 2018, 02.10.–05.10.2018, Riga (Latvia).
6. M. Kull, R. Zabels, **H. Seemen**, T. Jõgiaas, A. Tamm, Mechanical and optical properties of HfO_2/ZrO_2 nanolaminates grown using atomic layer deposition, 12th International Scientific Conference on Functional Materials and Nanotechnologies – FM&NT 2018, 02.10.–05.10.2018, Riga (Latvia).
7. A. Tamm, K. Kalam, M. Mikkor, T. Jõgiaas, **H. Seemen**, A. Šutka, K. Kukli, J. Link, R. Stern, S. Dueñas, H. Castán, Magnetic and electrical performance of atomic layer deposited nanocomposites, AVS 18th International Conference on Atomic Layer Deposition (ALD 2018), 29.07.–01.08.2018, Incheon (South Korea).
8. K. Kalam, **H. Seemen**, M. Mikkor, P. Ritslaid, R. Stern, S. Dueñas, H. Castán, A. Tamm, K. Kukli, Electric and magnetic properties of atomic layer deposited ZrO_2-HfO_2 thin films, AVS 18th International Conference on Atomic Layer Deposition (ALD 2018), 29.07.–01.08.2018, Incheon (South Korea).
9. K. Kalam, **H. Seemen**, P. Ritslaid, K. Kukli, A. Tamm, R. Stern, S. Dueñas, H. Castán, Magnetoelectric properties of atomic layer deposited ZrO_2-HfO_2 thin films, GSFMT Scientific Conference 2018, 07.03.–08.03.2018, Tallinn (Estonia).
10. K. Kalam, **H. Seemen**, P. Ritslaid, A. Tamm, M. Rähn, K. Kukli, A. Kasikov, J. Link, R. Stern, S. Dueñas, H. Castán, H. García, Atomic layer deposition of ZrO_2:Fe_2O_3 thin films, Joint EUROCVD 21 – Baltic ALD 15 Conference, 11.06.–14.06.2017, Linköping (Sweden).
11. K. Kalam, **H. Seemen**, P. Ritslaid, A. Tamm, M. Rähn, K. Kukli, A. Kasikov, J. Link, R. Stern, S. Dueñas, H. Castán, H. García, Atomic layer deposition of ZrO_2:Fe_2O_3 thin films, Functional Materials and Nanotechnologies – FM&NT-2017, 24.04.–27.04.2017, Tartu (Estonia).

12. K. Kalam, **H. Seemen**, P. Ritslaid, M. Rähn, A. Tamm, K. Kukli, A. Kasikov, J. Link, R. Stern, S. Dueñas, H. Castán, H. García, Atomic layer deposition of ZrO_2:Fe_2O_3 thin films, GSFMT Scientific Conference 2017, 07.03.–08.03.2017, Tartu (Estonia).
13. A. Tamm, K. Kalam, **H. Seemen**, P. Ritslaid, K. Kukli, J. Aarik, M. Heikkilä, J. Link, R. Stern, S. Dueñas, H. Castán, H. García, Atomic layer deposition and characterization of erbium-iron-oxide thin films, IEEE EDS Min-Colloquium, CDE 2017, Advanced Materials and Devices: Challenges and Opportunities: 11th Spanish Conference on Electron Devices, 8.02.–11.02.2017, Barcelona (Spain).
14. K. Kalam, **H. Seemen**, P. Ritslaid, A. Tamm, K. Kukli, A. Kasikov, J. Link, R. Stern, S. Dueñas, H. Castán, H. García, Atomic layer deposition of ZrO_2:Fe_2O_3 thin films, IEEE EDS Min-Colloquium, CDE 2017, Advanced Materials and Devices: Challenges and Opportunities: 11th Spanish Conference on Electron Devices, 8.02.–11.02.2017, Barcelona (Spain).
15. T. Jõgiaas, R. Zabels, **H. Seemen**, A. Tamm, K. Kukli, Atomic layer deposited thin films with gradient composition, ALD 2016 – the 16th International Conference on Atomic Layer Deposition, 24.07.–27.07.2016, Dublin (Ireland).
16. A. Tamm, T. Arroval, **H. Seemen**, K. Kukli, J. Aarik, H. García, S. Dueñas, H. Castán, M. Klaas, V. Jaks, Atomic layer deposition of tantalum oxide and titanium oxide laminates: characterization of growth process and resistive switching, ALD 2016 – the 16th International Conference on Atomic Layer Deposition, 24.07.–27.07.2016, Dublin (Ireland).

ELULOOKIRJELDUS

Nimi: Helina Seemen
Sünniaeg: 26.04.1993
E-mail: helina.seemen@ut.ee, helinaseemen@gmail.com

Hariduskäik

2017–...	Tartu Ülikool, doktoriõpe, materjaliteadus
2015–2017	Tartu Ülikool, magistriõpe, materjaliteadus
2012–2015	Tartu Ülikool, bakalaureuseõpe, füüsika
2009–2012	Rakvere Eragümnaasium, keskharidus (*cum laude*)

Töökohad ja ametid

01.08.2019–...	Karl Storz Video Endoscopy Estonia OÜ, valideerimisinsener (1,00)
18.10.2018–30.06.2019	Tartu Ülikool, Loodus- ja täppisteaduste valdkond, füüsika instituut, spetsialist (0,60)
01.05.2018–30.06.2018	Tartu Ülikool, Loodus- ja täppisteaduste valdkond, füüsika instituut, insener (0,60)
01.09.2017–30.04.2018	Tartu Ülikool, Loodus- ja täppisteaduste valdkond, füüsika instituut, insener (täiendava stipendiumi alusel)
01.01.2016–30.06.2017	Tartu Ülikool, Loodus- ja täppisteaduste valdkond, füüsika instituut, insener (0,40)
01.07.2015–31.12.2015	Tartu Ülikool, Loodus- ja tehnoloogiateaduskond, füüsika instituut, insener (0,40)
01.10.2014–30.06.2015	Tartu Ülikool, Loodus- ja tehnoloogiateaduskond, füüsika instituut, laborant (0,30)

Publikatsioonid

Kaheksateistkümmet teadusartikli viidet sisaldav publikatsioonide loetelu asub doktoriväitekirja “List of original publications and author’s contributions” ja “List of author’s other publications” peatükkides. Täiendav ja ajakohasem informatsioon publikatsioonide kohta on leitav aadressilt https://www.etis.ee/CV/Helina_Seemen/est.

Konverentsiettekanded

Suulised konverentsiettekanded, mille puhul olin esiautor:

1. **H. Seemen**, K. Kukli, A. Tamm, Properties of atomic layer deposited ZrO_2 or Fe_2O_3 based multilayers, AVS 21st International Conference on Atomic Layer Deposition (ALD 2021), 27.06.–30.06.2021, virtual meeting, virtual on-demand oral presentation (virtuaalne ettekanne).
2. **H. Seemen**, K. Kukli, A. Tamm, Magnetic properties of atomic layer deposited multilayer thin solid films, GSFMT Scientific Conference 2021, 14.06.–15.06.2021, Tartu (Estonia), virtual presentation (virtuaalne ettekanne).

3. **H. Seemen**, J. Link, R. Stern, T. Jõgiaas, K. Kukli, A. Tamm, Properties of atomic layer deposited iron and bismuth oxide layered structures, GSFMT Scientific Conference 2019, 04.02.–05.02.2019, Tartu (Estonia).
4. **H. Seemen**, M. Rähn, K. Kalam, T. Sajavaara, S. Dueñas, H. Castán, J. Link, R. Stern, K. Kukli, A. Tamm, Properties of atomic layer deposited zirconium and cobalt oxide nanolaminates, 12th International Scientific Conference on Functional Materials and Nanotechnologies – FM&NT 2018, 02.10.–05.10.2018, Riga (Latvia).
5. **H. Seemen**, M. Rähn, K. Kalam, T. Sajavaara, S. Dueñas, H. Castán, J. Link, R. Stern, K. Kukli, A. Tamm, Defect-induced effects in atomic layer deposited zirconium and cobalt oxide nanolaminates, The 2018 E-MRS Spring Meeting and Exhibit, 18.06.–22.06.2018, Strasbourg (France), invited talk.

Stendiettekanded, mille puhul olin esiautor:

1. **H. Seemen**, M. Rähn, T. Jõgiaas, J. Link, R. Stern, S. Dueñas, H. Castán, K. Kukli, A. Tamm, The importance of microscopic analysis on atomic layer deposited thin solid films, GSFMT Scientific Conference 2020, 04.02.–05.02.2020, Tallinn (Estonia).
2. **H. Seemen,** S. Dueñas, H. Castán, J. Link, R. Stern, T. Jõgiaas, K. Kukli, A. Tamm, Magnetic and electrical properties of atomic layer deposited iron oxide and bismuth oxide chloride layered structures, EuroCVD 22 – Baltic ALD 16 Conference, 24.06.–28.06.2019, Luxembourg (Luxembourg).
3. **H. Seemen,** M. Rähn, K. Kalam, S. Dueñas, H. Castán, J. Link, R. Stern, K. Kukli, A. Tamm, The properties of atomic layer deposited zirconium and cobalt oxide nanolaminates, GSFMT Scientific Conference 2018, 07.03.–08.03.2018, Tallinn (Estonia).
4. **H. Seemen,** K. Kalam, J. Kozlova, M. Rähn, V. Sammelselg, K. Kukli, A. Tamm, Using focused ion beam and transmission electron microscopy for examining thin film structures, Joint EUROCVD 21 – Baltic ALD 15 Conference, 11.06.–14.06.2017, Linköping (Sweden).
5. **H. Seemen,** T. Jõgiaas, A. Tamm, V. Sammelselg, The formation and distribution of cracks in bent atomic layer deposited coatings, ALD 2016 – the 16th International Conference on Atomic Layer Deposition, 24.07.–27.07.2016, Dublin (Ireland).
6. **H. Seemen,** T. Jõgiaas, R.-T. Kibur, Using atomic layer deposition for microtome blade cutting performance enhancement, The 13th International Baltic Conference on Atomic Layer Deposition – Baltic ALD 2015, 28.09.–29.09.2015, Tartu (Estonia).

Suulised ja stendiettekanded, mille puhul olin kaasautor:

1. K. Kalam, **H. Seemen**, M. Mikkor, T. Jõgiaas, P. Ritslaid, K. Kukli, A. Tamm, A. Kasikov, J. Link, R. Stern, S. Dueñas, H. Castán, Atomic layer deposition of ZrO_2-based thin films, GSFMT Scientific Conference 2020, 04.02.–05.02.2020, Tallinn (Estonia).

2. A. Tamm, A. Tarre, **H. Seemen**, K. Kukli, J. Link, R. Stern, Cupric oxide thin films grown by atomic layer deposition, EuroCVD 22 – Baltic ALD 16 Conference, 24.06.–28.06.2019, Luxembourg (Luxembourg).
3. K. Kukli, M. Kemell, M. J. Heikkilä, **H. Seemen**, K. Kalam, A. Tamm, H. Castán, S. Dueñas, J. Link, R. Stern, M. Ritala, M. Leskelä, Atomic layer deposition of metal oxide nanolaminates exhibiting nonlinear electrical and magnetic polarization with tunable resistivity, EuroCVD 22 – Baltic ALD 16 Conference, 24.06.–28.06.2019, Luxembourg (Luxembourg).
4. Ó. G. Ossorio, S. Dueñas, H. Castán, A. Tamm, K. Kalam, **H. Seemen**, K. Kukli, Resistive switching properties of atomic layer deposited ZrO_2-HfO_2 thin films, The 12th Spanish Conference on Electron Devices (CDE 2018), 14.11.–16.11.2018, Salamanca (Spain).
5. M. Mikkor, A. Šutka, **H. Seemen**, J. Merisalu, J. Link, R. Stern, S. Dueñas, H. Castán, K. Kukli, A. Tamm, Characterization of Bi_2O_3 film in compound with $MnFe_2O_3$ nanoparticles, 12th International Scientific Conference on Functional Materials and Nanotechnologies – FM&NT 2018, 02.10.–05.10.2018, Riga (Latvia).
6. M. Kull, R. Zabels, **H. Seemen**, T. Jõgiaas, A. Tamm, Mechanical and optical properties of HfO_2/ZrO_2 nanolaminates grown using atomic layer deposition, 12th International Scientific Conference on Functional Materials and Nanotechnologies – FM&NT 2018, 02.10.–05.10.2018, Riga (Latvia).
7. A. Tamm, K. Kalam, M. Mikkor, T. Jõgiaas, **H. Seemen**, A. Šutka, K. Kukli, J. Link, R. Stern, S. Dueñas, H. Castán, Magnetic and electrical performance of atomic layer deposited nanocomposites, AVS 18th International Conference on Atomic Layer Deposition (ALD 2018), 29.07.–01.08.2018, Incheon (South Korea).
8. K. Kalam, **H. Seemen**, M. Mikkor, P. Ritslaid, R. Stern, S. Dueñas, H. Castán, A. Tamm, K. Kukli, Electric and magnetic properties of atomic layer deposited ZrO_2-HfO_2 thin films, AVS 18th International Conference on Atomic Layer Deposition (ALD 2018), 29.07.–01.08.2018, Incheon (South Korea).
9. K. Kalam, **H. Seemen**, P. Ritslaid, K. Kukli, A. Tamm, R. Stern, S. Dueñas, H. Castán, Magnetoelectric properties of atomic layer deposited ZrO_2-HfO_2 thin films, GSFMT Scientific Conference 2018, 07.03.–08.03.2018, Tallinn (Estonia).
10. K. Kalam, **H. Seemen**, P. Ritslaid, A. Tamm, M. Rähn, K. Kukli, A. Kasikov, J. Link, R. Stern, S. Dueñas, H. Castán, H. García, Atomic layer deposition of ZrO_2:Fe_2O_3 thin films, Joint EUROCVD 21 – Baltic ALD 15 Conference, 11.06.–14.06.2017, Linköping (Sweden).
11. K. Kalam, **H. Seemen**, P. Ritslaid, A. Tamm, M. Rähn, K. Kukli, A. Kasikov, J. Link, R. Stern, S. Dueñas, H. Castán, H. García, Atomic layer deposition of ZrO_2:Fe_2O_3 thin films, Functional Materials and Nanotechnologies – FM&NT-2017, 24.04.–27.04.2017, Tartu (Estonia).
12. K. Kalam, **H. Seemen**, P. Ritslaid, M. Rähn, A. Tamm, K. Kukli, A. Kasikov, J. Link, R. Stern, S. Dueñas, H. Castán, H. García, Atomic layer deposition

of ZrO_2:Fe_2O_3 thin films, GSFMT Scientific Conference 2017, 07.03.–08.03.2017, Tartu (Estonia).

13. A. Tamm, K. Kalam, **H. Seemen**, P. Ritslaid, K. Kukli, J. Aarik, M. Heikkilä, J. Link, R. Stern, S. Dueñas, H. Castán, H. García, Atomic layer deposition and characterization of erbium-iron-oxide thin films, IEEE EDS Min-Colloquium, CDE 2017, Advanced Materials and Devices: Challenges and Opportunities: 11th Spanish Conference on Electron Devices, 8.02.–11.02.2017, Barcelona (Spain).
14. K. Kalam, **H. Seemen**, P. Ritslaid, A. Tamm, K. Kukli, A. Kasikov, J. Link, R. Stern, S. Dueñas, H. Castán, H. García, Atomic layer deposition of ZrO_2:Fe_2O_3 thin films, IEEE EDS Min-Colloquium, CDE 2017, Advanced Materials and Devices: Challenges and Opportunities: 11th Spanish Conference on Electron Devices, 8.02.–11.02.2017, Barcelona (Spain).
15. T. Jõgiaas, R. Zabels, **H. Seemen**, A. Tamm, K. Kukli, Atomic layer deposited thin films with gradient composition, ALD 2016 – the 16th International Conference on Atomic Layer Deposition, 24.07.–27.07.2016, Dublin (Ireland).
16. A. Tamm, T. Arroval, **H. Seemen**, K. Kukli, J. Aarik, H. García, S. Dueñas, H. Castán, M. Klaas, V. Jaks, Atomic layer deposition of tantalum oxide and titanium oxide laminates: characterization of growth process and resistive switching, ALD 2016 – the 16th International Conference on Atomic Layer Deposition, 24.07.–27.07.2016, Dublin (Ireland).

DISSERTATIONES SCIENTIAE MATERIALIS UNIVERSITATIS TARTUENSIS

1. **Martin Järvekülg**. Tubular microstructures by Hf-, Zr- and Ti-butoxide gel sheet rolling. Tartu, 2011, 112 p.
2. **Sergei Vlassov.** Investigation of nanoscale interactions and mechanical properties of nanostructures using quartz tuning fork based real-time measurements. Tartu, 2011, 171 p.
3. **Margus Kodu**. Pulsed Laser Deposition of Magnesium Oxide and Barium Ternary Oxides for Plasma Display Protective Layers. Tartu, 2011, 89 p.
4. **Rainer Pärna**. Surface studies of some oxide films. Tartu, 2011, 129 p.
5. **Jevgeni Šulga**. Self-assembly and interaction of nanostructures. Tartu, 2011, 114 p.
6. **Wojciech Kuznik**. Quantum-chemical computer simulations of the linear and non-linear optical properties of pyrazoloquinoline and dicyanopyrazine derivatives. Tartu, 2012, 89 p.
7. **Leonid Dorogin**. Structural and tribological properties of zero- and one-dimensional nanocrystals. Tartu, 2012, 193 p.
8. **Viljar Palmre**. Fabrication and characterization of microporous carbon-based electroactive polymer actuators. Tartu, 2012, 99 p.
9. **Madis Paalo**. Synthesis of CNT-metal oxide nanocomposites: sol-gel process, rheology, structural and functional properties. Tartu, 2014, 175 p.
10. **Raul Välbe**. Developement of ionic liquid composites by sol-gel method for elaboration of industrial nano- and microstructures. Tartu, 2014, 97 p.
11. **Urmas Joost**. Impurity and preparation dependent properties of titania thin films. Tartu, 2014, 155 p.
12. **Madis Umalas**. Application of sol-gel technology for production of ceramic nanocomposites and functional coatings. Tartu, 2015, 136 p.
13. **Elena Samsonova**. Energy transfer probe as a tool to study morphological and structural origins of fluorescence quenching in rare-earth doped nanophosphors. Tartu, 2015, 114 p.
14. **Jay Mondal**. Novel Corrosion Protective Nanostructured Composite Coatings. Tartu, 2016, 104 p.
15. **Kathriin Utt**. Metal oxide mesostructures for optical applications. Tartu, 2016, 88 p.
16. **Kaido Siimon**. Electrospun gelatin cross-linked by glucose. Tartu, 2016, 84 p.
17. **Marko Part**. Combined three-dimensional sol-gel structures and atomic layer deposited thin films. Tartu, 2017, 162 p.
18. **Pejman Rasti**. Analysis of Remote Sensing Image Super Resolution using Fluid Lenses. Tartu, 2017, 188 p.
19. **Ivo Romet**. Recombination luminescence of doped borates: origin and application prospects in dosimetry. Tartu, 2017, 111 p.

20. **Vladimir I. Kondratiev**. Processing and characterization of transparent electrode materials. Tartu, 2017, 111 p.
21. **Taivo Jõgiaas**. Mechanical properties of atomic layer deposited thin films and nanocomposites. Tartu, 2017, 125 p.
22. **Lauri Aarik**. Atomic layer deposition and characterization of thin oxide films for application in protective coatings. Tartu, 2017, 180 p.
23. **Triin Kangur**. Preparation and functional properties of stochastic micro-structured sol-gel silica materials. Tartu, 2018, 96 p.
24. **Marta Berholts**. Fragmentation of ionic and hydrogen-bonded molecules induced by synchrotron radiation. Tartu, 2018, 126 p.
25. **Priit Priimägi**. Development and optimization of 3D-microbatteries. Tartu, 2018, 118 p.
26. **Siim Hödemann**. Residual stress determination in chemically strengthened and thermally tempered glass plates using scattered light method. Tartu, 2019, 146 p.
27. **Jekaterina Kozlova**. Complex characterization of graphene structures on nanometer level. Tartu, 2019, 206 p.
28. **Kristjan Kalam**. Magnetic, electric and structural properties of atomic layer deposited zirconia-based nanolaminates and mixtures. Tartu, 2020, 94 p.
29. **Triinu Vihmann**. Ionic liquids: synthesis and application in lubrication and lithography. Tartu, 2020, 102 p.